Characteristics of Interannual Variability in Space-based XCO2 Global Observations

Yifan Guan[1], Gretchen Keppel-Aleks[1], Scott C. Doney[2], Christof Petri[3], Dave Pollard[4], Debra Wunch[5], Frank Hase[6], Hirofumi Ohyama[7], Isamu Morino[7], Justus Notholt[3], Kei Shiomi[9], Kim Strong[5], Rigel Kivi[10], Matthias Buschmann[3], Nicholas Deutscher[12], Paul Wennberg[11], Ralf Sussmann[8], Voltaire A. Velazco[12,13], Yao Té[14]

[1]Department of Climate and Space Sciences and Engineering, University of Michigan, Ann Arbor, MI, 48105, USA
[2]Department of Environmental Sciences, University of Virginia, Charlottesville, VA, 22903, USA
[3]Institute of Environmental Physics, Physics Department, University of Bremen, Bremen, 28359, Germany
[4]National Institute of Water and Atmospheric Research, Omakau, 9377, New Zealand
[5]Department of Physics, University of Toronto, Toronto, M5S 1A7, Canada
[6]Institute of Meteorology and Climate Research - Atmospheric Trace Gases and Remote Sensing, Karlsruhe Institute of Technology, Eggenstein-Leopoldshafen, 76344, Germany
[7]National Institute for Environmental Studies, Tsukuba, Ibaraki 305-0053, Japan
[8]Institute of Meteorology and Climate Research - Atmospheric Environmental Research, Karlsruhe Institute of Technology, Garmisch-Partenkirchen, 82467, Germany
[9]Earth Observation Research Center, Japan Aerospace Exploration Agency, Tsukuba, Ibaraki, 305-8505, Japan
[10]Space and Earth Observation Centre, Finnish Meteorological Institute, Sodankylä, 99600, Finland
[11]Divisions of Engineering and Applied Science and Geological and Planetary Science, California Institute of Technology, Pasadena, CA, 91125, USA
[12]Centre for Atmospheric Chemistry, School of Earth, Atmospheric and Life Sciences, University of Wollongong, Wollongong, 2522, Australia
[13]Deutscher Wetterdienst, Meteorological Observatory, Hohenpeissenberg, 82383, Germany
[14]Laboratoire d'Etudes du Rayonnement et de la Matière en Astrophysique et Atmosphères, French National Centre for Scientific Research, Paris, 75016, France

Correspondence to: Yifan Guan (guanyf@umich.edu)

Abstract. Atmospheric carbon dioxide (CO_2) accounts for the largest radiative forcing among anthropogenic greenhouse gases. There is, therefore, a pressing need to understand the rate at which CO_2 accumulates in the atmosphere, including the interannual variations (IAV) in this rate. IAV in the CO_2 growth rate is a small signal relative to the long-term trend and the mean annual cycle of atmospheric CO_2, and IAV is tied to climatic variations that may provide insights into long-term carbon-climate feedbacks. Observations from the Orbiting Carbon Observatory-2 (OCO-2) mission offer a new opportunity to refine our understanding of atmospheric CO_2 IAV since the satellite can measure over remote terrestrial regions and the open ocean where traditional in situ CO_2 monitoring is difficult, providing better spatial coverage compared to ground-based monitoring techniques. In this study, we analyze the IAV of column-averaged dry air CO_2 mole fraction (XCO_2) from OCO-2 between September 2014 to June 2021. The amplitude of IAV variations, which is calculated as the standard deviation of the timeseries, is up to 1.2 ppm over the continents and around 0.4 ppm over the open ocean. Across all latitudes, the OCO-2 detected XCO_2 IAV shows a clear relationship with ENSO-driven variations that originate in the tropics and are transported poleward. The similar zonal patterns of OCO-2 XCO_2 IAV timeseries compared to ground-based in situ observations and with column observations from the Total Carbon Column Observing Network (TCCON) and the Greenhouse Gases

Observing Satellite (GOSAT) provide validation that OCO-2 observations can be used reliably to estimate IAV. Furthermore, the extensive spatial coverage of the OCO-2 satellite data leads to smoother IAV timeseries than those from other datasets, suggesting that OCO-2 provides new capabilities for revealing small IAV signals despite sources of noise and error that are inherent to remote sensing datasets.

1 Introduction

Increasing atmospheric CO_2 concentration from anthropogenic emissions is the major driver of the observed warming of Earth's climate since the industrial revolution (IPCC, 2021). Although CO_2 accumulation in the atmosphere generally is ~45% of anthropogenic emissions on a multi-year average (Ciais et al., 2013; Friedlingstein et al., 2019), the growth rate shows substantial interannual variability (Conway et al., 1994). The difference between emissions and the atmospheric CO_2 growth rate results from net CO_2 uptake by oceans and terrestrial ecosystems (Prentice et al., 2001; Doney et al., 2009), and the fluctuations reflect variations in the strength of those sinks due to climate variations (Peters et al., 2017; Friedlingstein et al., 2019). Much research has suggested that interannual variability (IAV) in the growth rate is predominantly due to variations in terrestrial ecosystem carbon uptake (Marcolla et al., 2017), even though the average uptake is roughly comparable between land and ocean (Le Quéré et al., 2009). Existing atmospheric CO_2 observations from surface flask sampling and in situ networks have been used to estimate global- and regional-scale interannual variability in CO_2 fluxes (Gurney et al., 2003; Peylin et al., 2013; Keppel-Aleks et al., 2014; Piao et al., 2020). We note, however, that the surface observing network is located primarily on land and coastal sites, and more subtle ocean flux signals may be obscured by the large IAV in terrestrial fluxes.

Previous analyses of surface CO_2 IAV has shown a strong relationship with the phase and intensity of El Niño–Southern Oscillation (ENSO) (Le Quéré et al., 2009; Schwalm et al., 2011). ENSO variations originate from coupled ocean-atmosphere dynamics that are reflected in large wind and sea surface temperature anomalies over the central and eastern Pacific Ocean. ENSO affects the climate of much of the tropics and subtropics via atmospheric teleconnections on timescales of 2-7 years (Timmermann et al., 2018). On land, suppressed precipitation and high temperature associated with positive phases of ENSO (El Niño conditions) suppress CO_2 uptake by tropical ecosystems, while promoting fires that further reduce the CO_2 uptake by lands (Feely et al., 2002; McKinley et al., 2004; Piao et al., 2009; Wang et al., 2013). Although of smaller magnitude, the equatorial Pacific Ocean experiences weakening of the easterly trade winds and suppression of ventilation of deep, cold, carbon-rich waters to the surface during an El Ñino, reducing the efflux of natural CO_2 to the atmosphere (Patra et al., 2005 ; Chatterjee et al., 2017).

Chatterjee et al. (2017) were able to directly observe the ocean flux-driven signal on atmospheric CO_2 from El Ñino for the first-time using XCO_2 (column-averaged dry air CO_2 mole fraction) observed over the ocean by NASA's OCO-2 satellite. Space-based observations from OCO-2, which launched in July 2014, provide novel opportunities to characterize the patterns of IAV in XCO_2 in areas that were previously not directly observed by existing monitoring networks. The IAV in XCO_2 is being used implicitly for flux attribution in inverse modeling studies (Nassar et. al,

2011). These exciting results, however, must be tempered by an awareness that atmospheric CO_2 IAV is a relatively small signal. For example, IAV in the surface network is about 1 ppm in scale compared to a seasonal amplitude of around 10 ppm in northern high latitudes. OCO-2 measures column averaged CO_2, so its measurements are sensitive to variations in the boundary layer mole fraction, which is in direct contact with the land or atmospheric fluxes, but also variations in the free troposphere and stratosphere, where flux signals are generally smaller than those observed at the surface (Olsen and Randerson, 2004). Furthermore, variations in the free troposphere are expected to have relatively long correlation length scales due to efficient mixing, making it important to consider the spatial scales at which XCO_2 observations provide unique information. This is especially important in light of analysis which suggests that the error variance budget in OCO-2 observations is large and contains substantial spatially coherent signal (Baker et al., 2022; Torres et al., 2019; Mitchell et al., 2023).

In this paper, we analyze XCO_2 from OCO-2 to characterize spatiotemporal patterns in IAV at near-global scale, over both land and ocean, and relate XCO_2 variations to ENSO conditions. We contextualize the information contained in OCO-2 observations by comparing with space-based GOSAT and ground-based TCCON XCO_2 and with surface measurements of CO_2. Finally, we use these comparisons to emphasize the spatial scales at which the IAV signal emerges from instrumental noise.

2 Data and Methods

2.1 Datasets

2.1.1 OCO-2 observatory

We analyzed IAV in dry air, column-average mole fraction XCO_2 inferred from OCO-2 satellite observations. The OCO-2 observatory was launched in July 2014 and has measured passive, reflected solar near infrared CO_2 and O_2 absorption spectra using grating spectrometers since September 2014 (Eldering et al., 2017). XCO_2 data are retrieved from the measured spectra using the Atmospheric CO_2 Observations from Space (ACOS) optimal estimation algorithm, which is a full physics algorithm that takes into account XCO_2 and other physical parameters, including surface pressure, surface albedo, temperature, and water vapor profile in its state vector (Crisp et al., 2010; O'Dell et al., 2018). The satellite flies in a polar and sun-synchronous orbit that repeats every 16 days, with three different observing modes of OCO-2, namely nadir (land only, views the ground directly below the spacecraft), glint (over ocean and land, views just off the peak of the specularly reflected sunlight), and target (typically for comparison with specific ground-based or airborne measurements) (Crisp et al., 2012; Crisp et al., 2017). We use the version 10 OCO-2 Level 2 bias-corrected XCO_2 data product from Goddard Earth Sciences Data and Information Services Center (GES DISC) Archive: https://disc.gsfc.nasa.gov/datasets/OCO2_L2_Lite_FP_10r/summary), which has been validated with collocated ground-based measurements from the Total Carbon Column Observing Network (TCCON; discussed in more detail in Section 2.2). After filtering and bias correction, the OCO-2 XCO_2 retrievals agree well with TCCON in nadir, glint, and target observation modes, and generally have absolute median differences less than 0.4 ppm and Root Mean Square differences less than 1.5 ppm (O'Dell et al., 2018; Wunch et al., 2017).

2.1.2 TCCON

We corroborate patterns of XCO₂ IAV from OCO-2 with those from TCCON, a ground-based network of Fourier transform spectrometers that measure direct solar absorption spectra in the near infrared (Wunch et al., 2011).

115   Retrievals of XCO₂ and other gases are computed using the GGG algorithm, a nonlinear least-squares spectral fitting algorithm. The TCCON retrievals are tied to the World Meteorological Organization (WMO) X2007 CO₂ scale via calibration with aircraft and AirCore profiles above the TCCON sites (Karion et al., 2010; Wunch et al., 2010). This ensures an accuracy and precision of ~0.6 ppm(1sigma) throughout the network (Washenfelder et al., 2006; Messerschmidt et al., 2010; Deutscher et al., 2010, Wunch et al., 2010). TCCON has been used widely as a validation

120   standard by providing independent measurements to compare with multiple satellite XCO₂ retrievals including OCO-2. In previous work Sussmann and Rettinger (2020) have demonstrated a concept to retrieve annual growth rates of XCO₂ from TCCON data, which are regionally to hemispherically representative in spite of the non-uniform sampling in time and space inherent to the ground-based network. In our study, we focus on IAV in the XCO₂ timeseries from 26 TCCON sites (Table 1, Fig.1) that have at least 3 years of observational coverage within the period from September

125   2014 to June 2021. These TCCON data have been filtered using the standard filter that is based on a measure of cloudiness and limits the solar zenith angle. Data are publicly available from the TCCON GGG2014 Data Archive (https://tccondata.org/) hosted by the California Institute of Technology.

Table 1. TCCON Column-Averaged Dry-Air Mole Fractions of CO₂ (GGG2014 Data)

130

Region	Site	Acronym	Latitude	Longitude	Start Date	End Date	Publication
Polar Northern Hemisphere (60-90°N)	Eureka (NU)	eu	80.05	-86.42	2010-07	2020-07	Strong, K. et al., 2017
	Ny Ålesund	sp	78.90	11.90	2014-04	2019-09	Notholt, J. et al., 2019
	Sodankylä (FI)	so	67.37	26.63	2009-05	2020-10	Kivi, R. et al., 2017
Temperate Northern Hemisphere (20-60°N)	East Trout Lake(SK)	et	54.35	-104.99	2016-10	2020-09	Wunch, D., et al., 2017
	Bialystok (PL)	bi	53.23	23.03	2009-03	2018-10	Deutscher, N. et al., 2017
	Bremen (DE)	br	53.10	8.85	2010-01	2020-06	Notholt, J. et al., 2017
	Karlsruhe (DE)	ka	49.10	8.44	2010-04	2020-11	Hase, F. et al., 2017
	Paris (FR)	pr	48.97	2.37	2014-09	2020-06	Te, Y. et al., 2017
	Orléans (FR)	or	47.97	2.11	2009-08	2020-06	Warneke, T. et al., 2017
	Garmisch (DE)	gm	47.48	11.06	2007-07	2020-06	Sussmann, R. et al., 2017
	Zugspitze (DE)	zs	47.42	10.98	2015-04	2020-06	Sussmann, R. et al., 2018
	Park Falls (US)	pa	45.95	-90.27	2004-06	2020-12	Wennberg, P. O. et al., 2017
	Rikubetsu (JP)	rj	43.46	143.77	2013-11	2019-09	Morino, I. et al., 2017
	Lamont (US)	oc	36.60	-97.49	2008-07	2020-12	Wennberg, P. O. et al., 2017
	Anmyeondo (KR)	an	36.58	126.33	2015-02	2018-04	Goo, T.-Y. et al., 2017
	Tsukuba (JP)	tk	36.05	140.12	2011-08	2019-09	Morino, I. et al., 2017
	Edwards (US)	df	34.96	-117.88	2013-07	2020-12	Iraci, L. et al., 2017
	Caltech (US)	ci	34.14	-118.13	2012-09	2020-12	Wennberg, P. O. et al., 2017
	Saga (JP)	js	33.24	130.29	2011-07	2020-12	Shiomi, K.et al., 2017
	Izana (ES)	iz	28.30	-16.50	2007-05	2021-02	Blumenstock, T. et al., 2017

Tropical Northern Hemisphere (0-20°N)	Burgos (PH)	bu	18.53	120.65	2017-03	2020-03	Morino, I., et al., 2018
Tropical Southern Hemisphere (0-20°S)	Ascension Island (SH)	ae	-7.92	-14.33	2012-05	2018-10	Feist, D. G. et al., 2017
	Darwin (AU)	db	-12.46	130.94	2005-08	2020-04	Griffith, D. W. T., et al., 2017
Temperate Southern Hemisphere (20-60°S)	Réunion Island (RE)	ra	-20.90	55.49	2011-09	2020-07	De Maziere, M. et al., 2017
	Wollongong (AU)	wg	-34.41	150.88	2008-06	2020-06	Griffith, D. W. T. et al., 2017
	Lauder (NZ)	ll	-45.04	169.68	2010-02	2018-10	Sherlock, V. et al., 2017
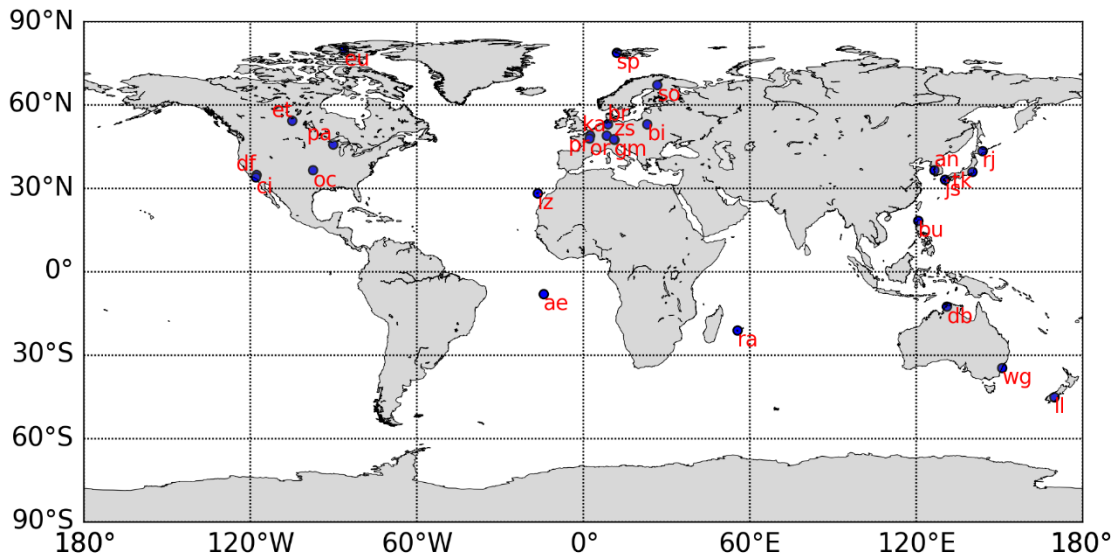
Figure 1. Map showing the locations and the acronyms of the TCCON sites.

2.1.3 Marine Boundary Layer Observations

To explore differences in surface and column-average CO_2 IAV, we analyze IAV in the surface CO_2 mole fraction at marine boundary layer (MBL) sites in the NOAA (National Oceanic and Atmospheric Administration) cooperative sampling network(https://gml.noaa.gov/dv/site/?program=ccgg). At these sites, boundary layer CO_2 is measured using weekly flask samples (Masarie and Tans, 1995; Dlugokencky et al., 2016). MBL sites are typically far away from anthropogenic sources and regions of active terrestrial exchange, so they provide an estimate for large-scale patterns in the global background CO_2 concentration. The surface MBL dry air mole fraction data has an accuracy level of about 0.1 ppm. In this study, we select 16 sites with at least 80% data coverage for the approximately 7-year period overlapping with OCO-2 (Table 2, Fig.2), and the data are aggregated into four north-south zones for comparison with OCO-2 XCO2: northern and southern hemisphere tropical (0 - 20°) and Northern Hemisphere/Southern Hemisphere extratropical zones (20-60°). Each belt contains at least three MBL sites. Higher

latitudes (60-90°) are not considered in this comparison due to the gaps remaining in the OCO-2 XCO_2 record in high latitudes during wintertime and shouldering seasons.

Table 2. Marine Boundary Layer stations within the NOAA Earth System Research Laboratory CO₂ sampling network

Region	Station	Acronym	Latitude	Longitude	Start Date	End Date
Temperate Northern Hemisphere (20-60°N)	Mace Head, Ireland	MHD	53.3	-9.9	2014-01	2020-07
	Shemya, AK	SHM	52.7	174.1	2014-01	2020-07
	Terceira Island Azores	AZR	38.8	-27.4	2014-01	2020-07
	Tudor Hill, Bermuda	BMW	32.3	-64.9	2014-01	2020-07
	Sand Island, Midway	MID	28.2	-177.4	2014-01	2020-07
	Key Biscayne, FL	KEY	25.7	-80.2	2014-01	2020-07
Tropical Northern Hemisphere (0-20°N)	Cape Kumukahi, HI	KUM	19.5	-154.8	2014-01	2020-07
	Mariana Islands, Guam	GMI	13.5	144.7	2014-01	2019-08
	Ragged Pointed, Barbados	RPB	13.2	-59.4	2014-01	2020-07
	Christmas Island, Republic of Kiribati	CHR	1.7	157.2	2014-01	2019-08
Tropical Southern Hemisphere (0-20°S)	Seychelles	SEY	-4.7	55.2	2014-01	2020-07
	Ascension Island	ASC	-8.0	-14.4	2014-01	2020-07
	Tutuila, America Samoa	SMO	-14.2	-170.6	2014-01	2020-07
Temperate Southern Hemisphere (20-60°S)	Cape Grim, Australia	CGO	-40.7	144.7	2014-01	2020-07
	Baring Head	BHD	-41.4	174.9	2014-01	2020-07
	Crozet Island	CRZ	-46.5	51.9	2014-01	2020-07
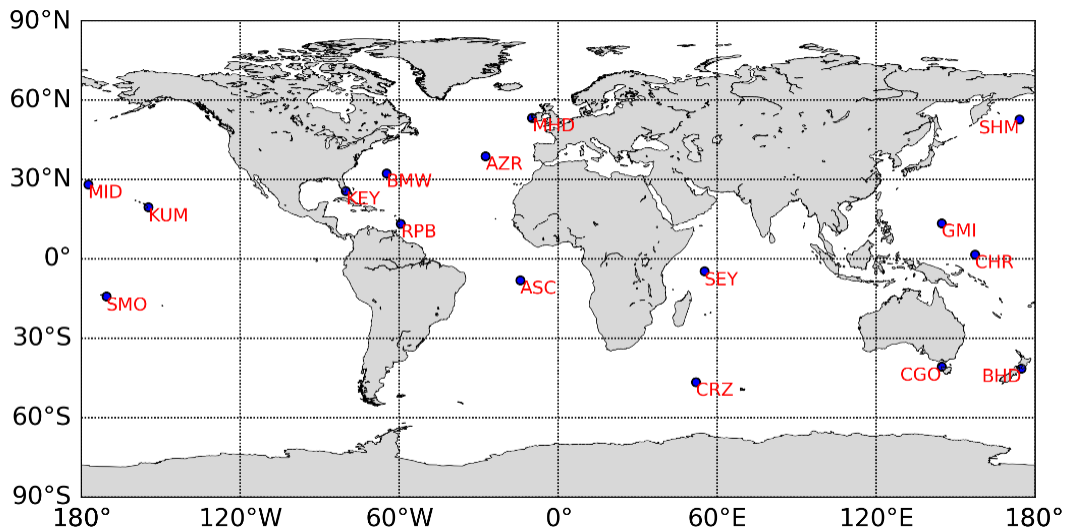
Figure 2. Map showing the locations and the acronyms of the Marine Boundary Layer stations within the NOAA Earth System Research Laboratory CO2 sampling network.

2.1.4 GOSAT

We compare patterns of XCO_2 IAV from OCO-2 with those from GOSAT. Also known as Ibuki, GOSAT is the world's first satellite dedicated to greenhouse gas monitoring, measuring global total column CO_2 and CH_4 since 2009.

With the Thermal and Near infrared Sensor for carbon Observation (TANSO) - Fourier Transform Spectrometer (FTS) onboard for greenhouse gas monitoring using three SWIR bands and one TIR band (Cogan et al., 2012; Yoshida et al., 2013). Column-averaged dry mole fraction are obtained at a circular footprint of approximately 10.5 km. GOSAT has a regional biased of about approximately 0.3 ppm and 1.7 ppm single observation error versus the TCCON (Kulawik et al., 2016). We utilize the FTS SWIR Level 3 data global monthly 2.5° resolution mean CO_2 mixing ratio products from 2009 June to 2021 December to generate IAV and make comparisons with OCO-2. L3 products are generated by interpolating, extrapolating, and smoothing the FTS SWIR column-averaged mixing ratios of CO2 and apply the geostatistical calculation technique Kriging method. GOSAT observation datasets are available to public at NIES GOSAT website (https://www.gosat.nies.go.jp/en/about_5_products.html).

2.1.5 Multivariate ENSO Index (MEI)

We use the bi-monthly Multivariate El Niño/Southern Oscillation (ENSO) index (MEI; downloaded from Physical Sciences Laboratory: https://psl.noaa.gov/enso/mei/) to explore the relationship between CO_2 IAV and ENSO. The MEI is the time series of the leading combined Empirical Orthogonal Function of five different variables (sea level pressure, sea surface temperature, zonal and meridional components of the surface wind, and outgoing longwave radiation) over the tropical Pacific basin. Positive values in the MEI indicate El Niño conditions, while negative values indicate La Niña conditions, and the magnitude reflects the relative strength. Unlike other ENSO indices which use only one climate metric (e.g., the sea level pressure difference between Tahiti and Darwin or the sea surface temperature anomaly within a pre-defined box), the MEI provides for a more complete and flexible description of the ENSO phenomenon than traditional single variable ENSO indices and has less vulnerability to errors (Klaus Wolter et. al, 2011).

2.2 Methods

2.2.1 Spatial Aggregation

We aggregate daily XCO_2 observations from the version 10 OCO-2 Level 2 lite product to monthly scale, exploring patterns of IAV at three spatial scales: gridcell-level, zonal averages over 5° of latitude, and broad zonal belts. Aggregating soundings reduces random noise in the observations, mitigates the impact of data gaps due to cloud cover, and partly mitigates effect from low winter sunlight levels in polar regions. For gridcell level analysis, we aggregate data equatorward of 45° to 5°x5° bins since these data are not limited by polar night or degraded by high solar zenith angles during winter. Poleward of 45° in both hemispheres, we aggregate the satellite observation to a latitude-longitude resolution of 5°x10° to compensate for fewer and noisier soundings in these latitudes, especially during winter and its shoulder seasons. Within each 5°x5° or 5°x10° gridcell, only months that have more than 5 soundings are included in the analysis. Our criteria for aggregation are based on sensitivity experiments in which we modulated the grid cell resolution from 1°x1° to 15°x15° (Fig. S1 and Fig. S2) and varied the threshold on the required number of soundings within a month from 1 to 25 (Fig. S3, Fig. S4 and Fig. S5). Our goal was to reduce noise but maintain high spatial coverage (Fig. S6 and Fig. S7). The 5°x5° and 5°x10° aggregation strike the necessary balance of reducing

noise (evidenced by the smoother IAV amplitude fields as aggregation increases in Fig. S1) but maintaining spatial information by not oversmoothing (evidenced by the fact that the aggregation occurs at spatial scales finer than the "elbow" where correlations among 1° gridcells stop changing with separation distance in Fig. S8)

In our analysis, we also aggregate data to zonal averages. At intermediate spatial scales, we average all data around the 5° latitude bins described above. For comparison with TCCON and MBL data, which are spatially sparse, we further aggregate XCO_2 data into four broad zonal belts – each of which contains at least 1 TCCON or 3 MBL stations -- (delineated in Table.1 and Table.2) to assess IAV patterns among the datasets. Keppel-Aleks et al., (2014) showed that drivers of IAV (i.e., temperature, drought stress, or fire) could be attributed when surface CO_2 were aggregated into similar broad zonal belts, whereas process-level attribution was not possible with global averaging. We therefore analyze broad zonal belts to gain a large-scale understanding of how three CO_2 datasets are similar and where differences lie.

2.2.2 Deriving interannual variations

We use a consistent process to calculate IAV (Equation 1) from the raw OCO-2, TCCON and MBL timeseries. The methodology is based on approaches used in Keppel-Aleks et al. (2013) and NOAA curve fitting methodology (Thoning et al, 1989). We decompose the raw time-series data into a long-term trend (which is a function of location (x,y) and time (t)), a seasonal cycle (which is a function of location and calendar month (m)), and IAV anomalies using Equation 1:

$$IAV(x,y,t) = Raw(x,y,t) − Trend(x,y,t) − Seasonal(x,y,m) \qquad \text{Equation 1}$$

We first fit a third order polynomial to the Raw timeseries to calculate the observed trend at each location (Fig. 3a). After removing the trend calculated at each gridcell (Fig. 3b), we calculate a mean seasonal cycle by taking the mean value of all January, February, etc. data (Fig. 3c). Particularly at high latitudes, some months are systematically under sampled. For these gridcells, we must have at least two years with sufficient observations to calculate a climatological mean for that month, otherwise, that calendar month is assumed to have insufficient data to infer the IAV. Finally, we remove the mean seasonal cycle from the detrended timeseries at each gridcell to obtain the IAV anomaly timeseries (Fig. 3d). Given the short data record, we quantify the uncertainty in our calculation of the climatological seasonal cycle as the standard error for each calendar month (blue shading in Fig. 3c), and this uncertainty is propagated to the corresponding IAV timeseries (Fig. 3d). We fit a third order polynomial to the raw timeseries since the GOSAT,MBL

and TCCON timeseries extend over a decade in length. We confirm that the use of a third-order polynomial, versus a
second-order polynomial, does not remove the IAV signal from the shorter OCO-2 timeseries (Fig. S9).
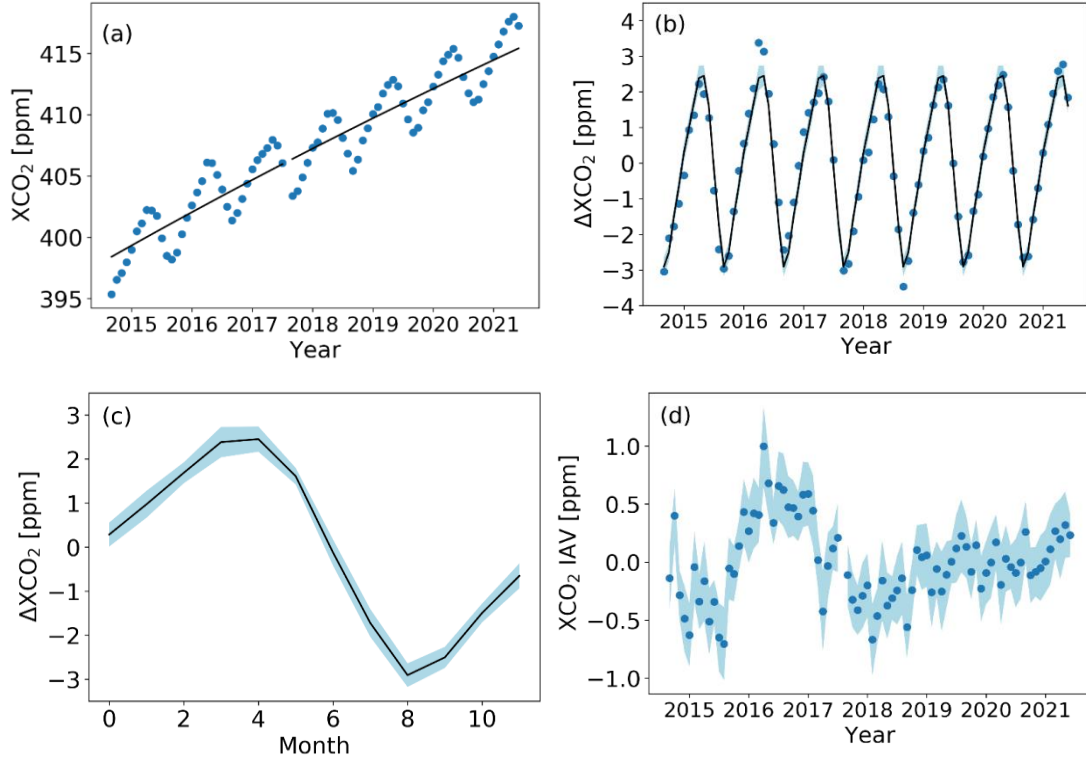
Figure 3. Methodology to calculate the CO_2 interannual variability timeseries, using OCO-2 XCO_2 data at the 5° grid cell at 20°N, 155°W, which contains Moana Loa, as an example. (a) 5°resolution monthly mean raw OCO-2 XCO_2 and the associated 3rd order polynomial trend. (b) detrended monthly XCO_2 after removing the long-term trend with a repeating 12-month annual cycle obtained from calculating the mean for each month. The light blue shading gives the uncertainty of the seasonal cycle, which is derived by calculating the standard deviation across all Januarys, Februarys, etc. (c) 12-month mean annual cycle together with the uncertainty range plotted in (b). (d) Resulting interannual variability, when mean annual cycle is removed from detrended timeseries.

3 Results

3.1 Spatiotemporal Variations based on OCO-2 observation

When averaged into broad zonal belts representing the tropics and mid-latitudes, the OCO-2 XCO_2 IAV timeseries anomalies range between -0.5 to 0.75 ppm (Fig. 4a). All latitude bands show increasing IAV during positive MEI (El Niño) and decreasing IAV during negative MEI (La Niña), although the phasing varies among latitudes. During the strong 2015–2016 El Niño, which began around March 2015 and reached its peak at the start of 2016, XCO_2 showed the largest IAV. The Southern Hemisphere extratropical regions have larger and more rapid response in the IAV associated with ENSO compared to other zones, especially for the smaller El Niño that peaked at the beginning of 2020. At this time, the XCO_2 IAV timeseries had an anomaly nearly twice as large as other latitude belts (Fig. 4). During both El Niño events, the IAV timeseries in the NH tropics zone peaks nearly six months after the maximum MEI value.

270

We assess the spatial correlation patterns between the IAV timeseries and MEI (Fig. 8a). The XCO$_2$ IAV timeseries have strong correlation coefficient with the MEI index in both Southern Hemisphere and Northern Hemisphere low latitudes from 0° to 30°N at lag 0, whereas in the Northern Hemisphere extratropics, the maximum positive correlation occurs at month 4 (Fig. 8b). The positive correlation between MEI and the IAV timeseries is gradually attenuated,

275   with no clear correlation at six months lag (Fig. 8c).

280

285

290

295

300

305

310
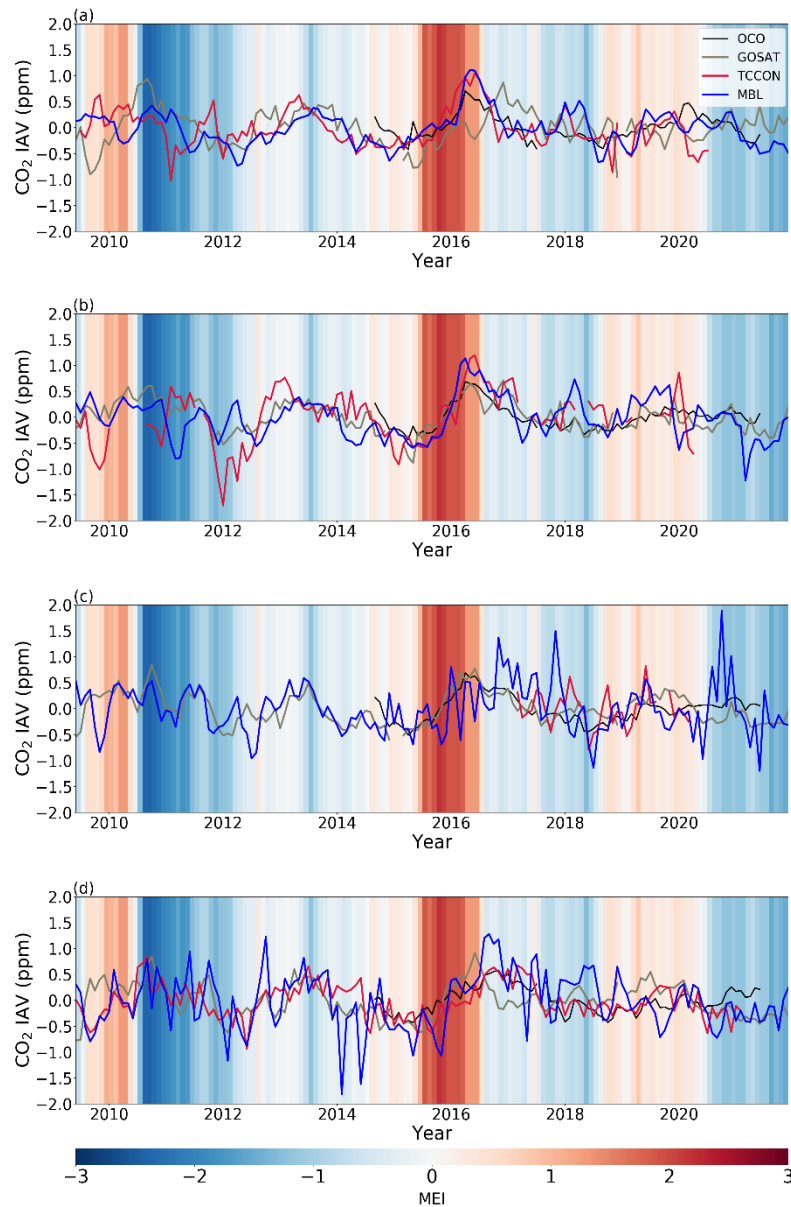
Figure 4. IAV timeseries averaged for zonal bands between 60 °N and 60 °S from three different observing strategies. (a) Space-based OCO-2 XCO₂, (b) Surface CO₂ observations from NOAA's marine boundary layer (MBL) sites, (c), Ground-based TCCON XCO₂, (d) Space-based GOSAT XCO₂. For all panels, the background shading indicates the Multivariate ENSO Index (MEI), which is positive during El Ñino phases.

315 The differences in temporal phasing between the broad zonal belts (Fig. 4a) associated with El Niño events can be linked to transport of El Ñino-driven CO_2 flux anomalies away from the tropics when zonal means are calculated from OCO-2 observations at 5° latitude resolution (Fig. 5). For the two El Ñino periods in 2015-2017 and late-2018 to 2021, high IAV values originate in the tropics and a smooth transition to high IAV values is seen at higher latitudes as time progresses (Fig. 5a). We note that fluxes outside the tropics may also be influenced by ENSO-related climate

320 variability, yet the transport of tropical-driven anomalies appears to dominate. This 7-year study period also captures the half-year lags for atmospheric transport or climate-ecological teleconnections that impacts XCO_2 variations in the far North. While the OCO-2 patterns largely conform with variability expected based on ENSO and are in broad agreement with other observational networks, there are some anomalies that cannot be explained, such as the high XCO_2 in early 2020 around 60°S. Even with more aggressive data filtering, this episode persists, requiring more

325 investigation of unknown geophysical drivers of high XCO_2 or potential retrieval issues that could cause a high bias.
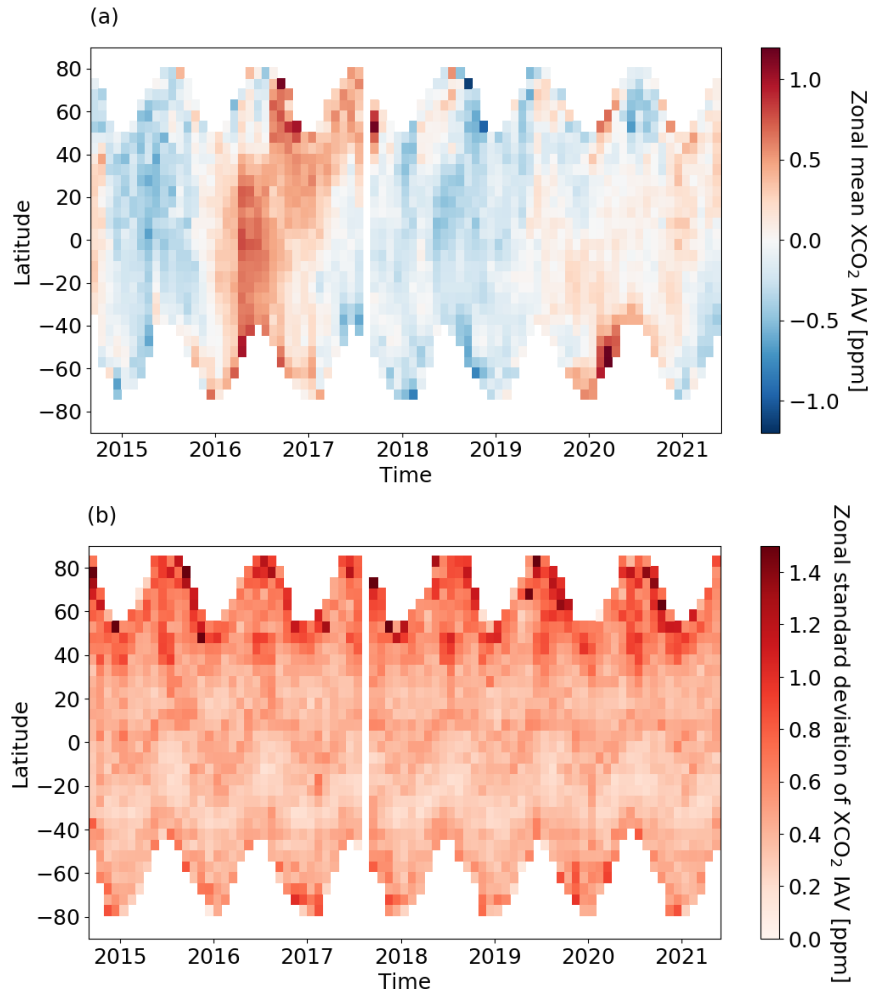
Figure 5. Hovmöller Diagrams diagram showing zonal mean OCO-2 XCO₂ IAV timeseries for 5° latitude bins (a) and the zonal standard deviation of XCO₂ IAV (b), which gives an estimate of coherence in the IAV patterns among grid cells in the 5° zonal belt.

We quantify coherence in CO_2 IAV within a latitude circle by taking the standard deviation across gridcell-level IAV anomalies within each 5° latitude zone. The standard deviation among gridcells is highest in the far North, with values as high as 1 ppm poleward of 45°N and as low as 0.2 ppm in the Southern Tropical bands (Fig. 5b), indicating that IAV is less spatially coherent in the Northern Hemisphere. This may be consistent with studies that show greater IAV in terrestrial ecosystem fluxes (concentrated in the northern hemisphere) (Zeng et al., 2005) relative to ocean fluxes, or may reflect that our IAV timeseries also retains the imprint of sampling, measurement, and retrieval errors, which become more pronounced at higher latitudes. In general, there is not a time-dependent or ENSO-related pattern for the longitudinal variation of IAVs (no obvious changes during the two El Ñino periods), which suggests the variation within each 5° band may be approximately stable and does not change substantially with interannual climate events.
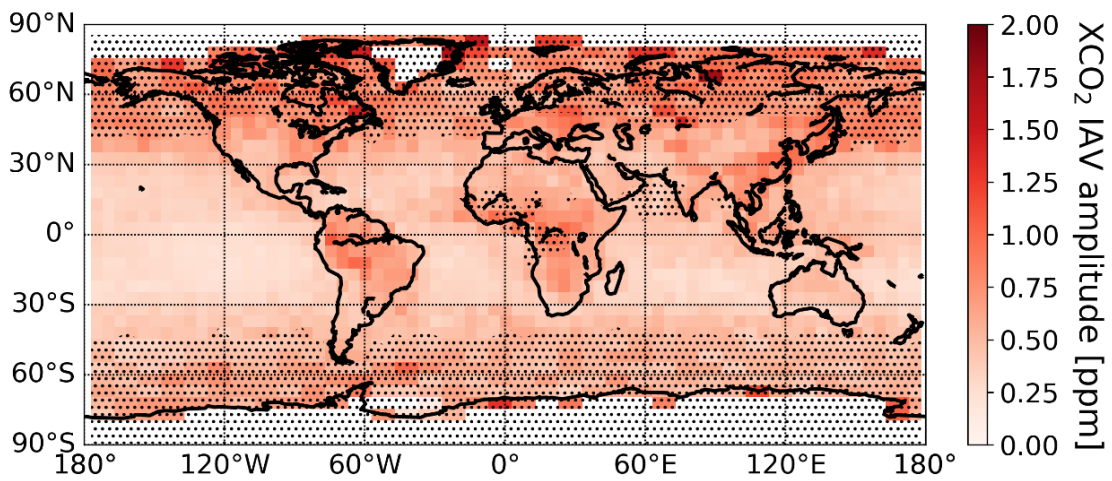
Figure 6. OCO-2 XCO₂ IAV amplitude, determined as the standard deviation of the IAV timeseries. Data equatorward of 45° are averaged at 5°by 5° resolution , and data poleward of 45° are averaged at 5°by 10° resolution. Shaded regions indicate gridcells that lack mean annual cycle data for at least two calendar months due to polar night or related retrieval challenges.
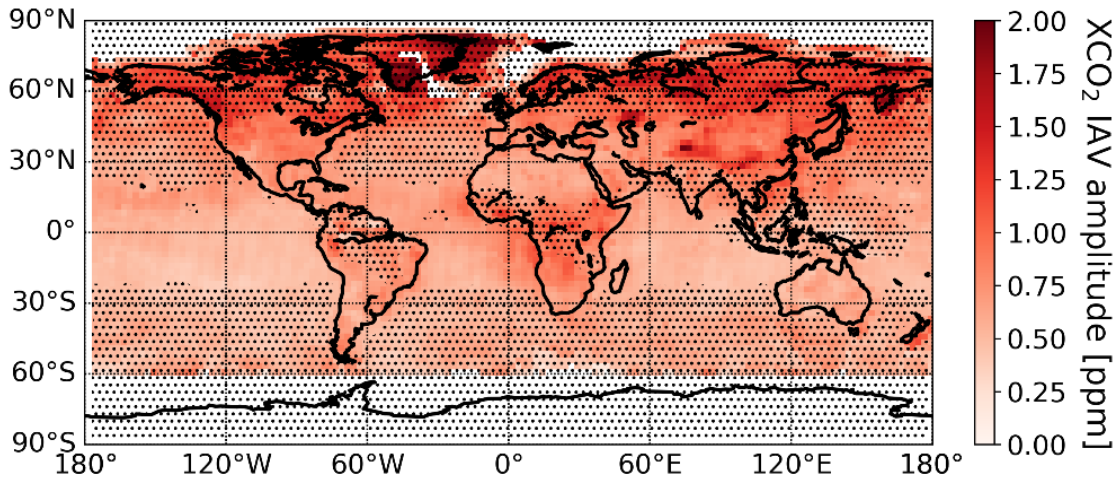
Figure 7. Similar as Figure 6 but based on GOSAT data.

375
380
385
390
395
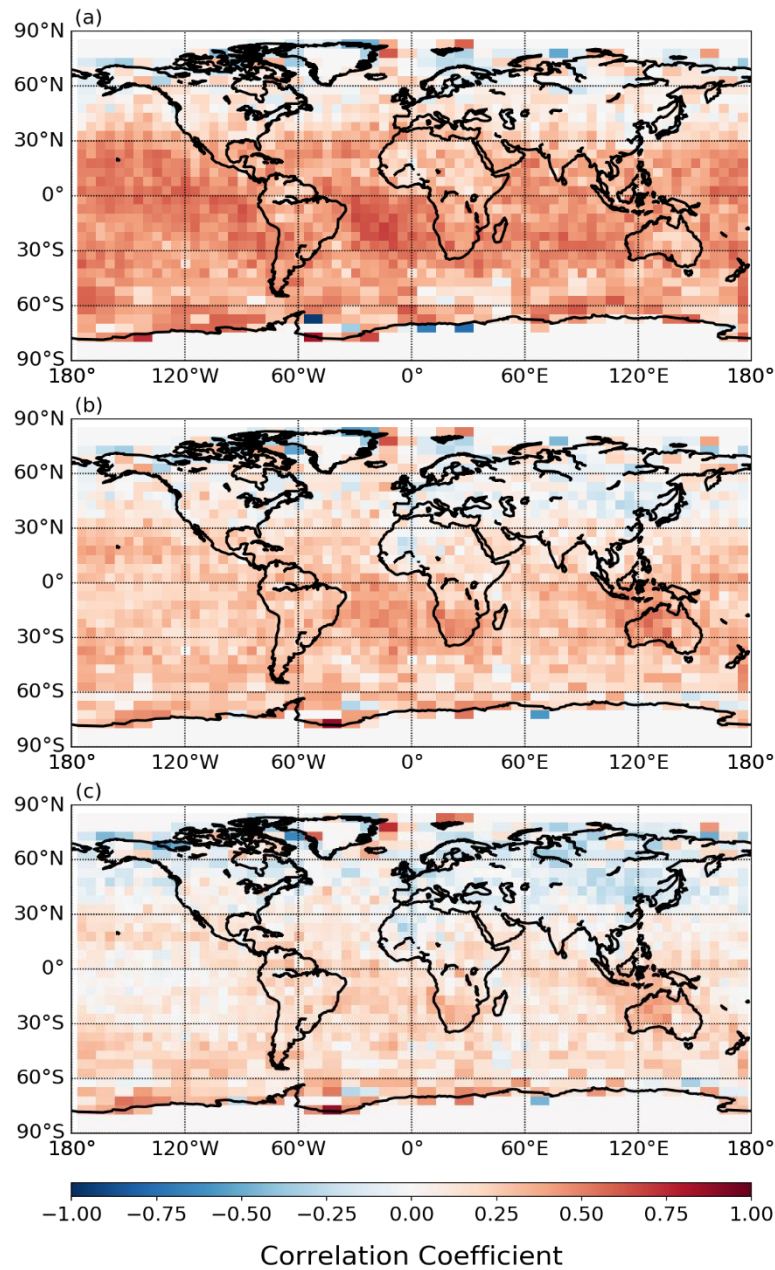
Figure 8. Correlation coefficient between local grid cell OCO-2 XCO₂ IAV timeseries and MEI .

400

The XCO₂ IAV amplitude (the standard deviation of the IAV timeseries) is notably larger over continental gridcells compared to ocean gridcells (Fig. 6). In both hemispheres, the IAV amplitude over subtropical ocean basins is less than 0.4 ppm, while the IAV amplitude over tropical land in Southeast Asia, Congo forests and Amazon Basin is about 1 ppm. In higher latitudes, the XCO₂ IAV amplitude can exceed 1.2 ppm above deciduous and boreal forests in North America and Eurasia. Higher values over land likely occur due to the active CO₂ exchange between terrestrial ecosystem and the atmosphere, but we cannot rule out that retrievals over land show more variance due to complex topography, albedo, etc., which are elements of the retrieval state vector. Nevertheless, over land areas with low carbon

405

exchange (e.g., Australia, the Middle East, the Sahara Desert), the XCO₂ IAV amplitude is nearly of the same low
level as the ocean basins. It is worth noting that for high latitude regions, including both Northern continents and
Southern Ocean, OCO-2 does not obtain observations over a full calendar year (stippled gridcells in Fig. 6) due to
polar nights, low light levels, and high solar zenith angles. The XCO₂ IAV amplitudes are less zonally coherent
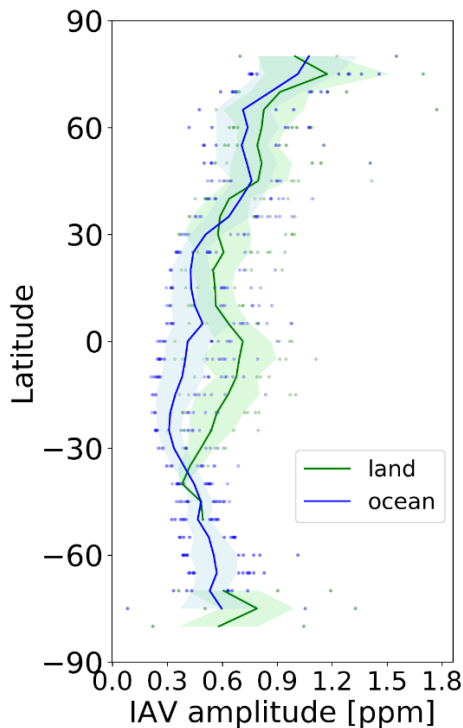
**Figure 9. Latitudinal profile for zonal mean of IAV amplitude and the standard deviation among land (green) or ocean
(blue) gridcells in each latitude band (shaded area). Individual points represent all grid cells valid IAV record within the
certain zonal band.**
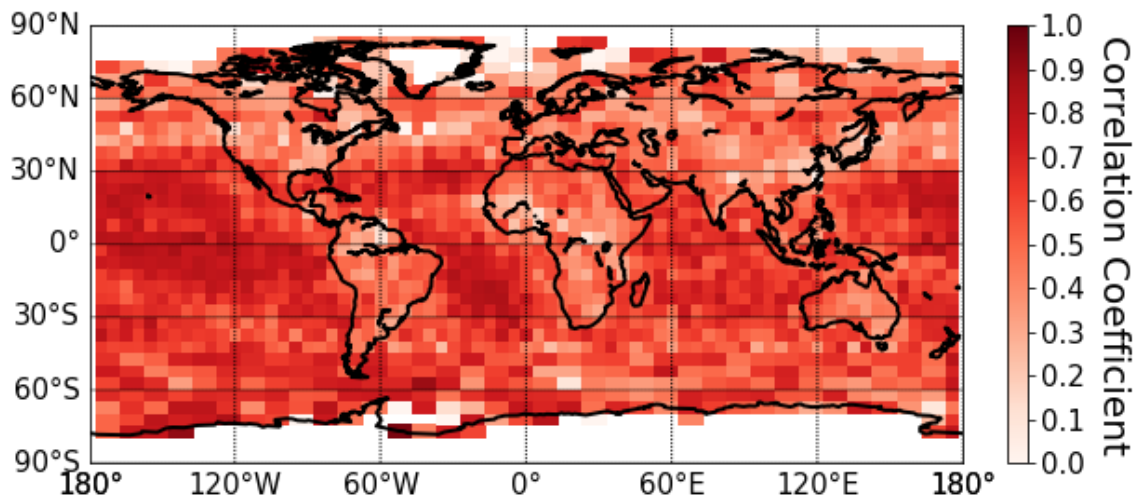
**Figure 10. Correlation coefficient between local grid cell IAV timeseries and the corresponding 5° zonal mean XCO₂ IAV
timeseries.**

420   through these regions than those in the tropics and mid-latitudes, for both land and ocean. When averaging all ocean or land grid cells around a latitude circle, the zonal mean IAV amplitude over the ocean ranges from 0.3 to 1.0 ppm, while the land IAV amplitude ranges from 0.4 to 1.1 ppm (Fig. 9). Both the land and ocean profiles have similar north-south patterns, with higher IAV amplitude in the Northern Hemisphere and lower IAV amplitude in the Southern Hemisphere, and the small IAV amplitudes in the subtropics of both hemispheres, with more scatter among land

425   gridcells than ocean (Fig. 5b and Fig. 9), suggesting either the influence of local flux IAV on land or greater error associated with retrievals on land. We note better coherence between the XCO_2 IAV timeseries of each local grid cell and that of zonal mean XCO_2 IAV timeseries for ocean, with correlation coefficients of approximately 0.8. In contrast, land gridcells are generally correlated with the zonal mean at around 0.4 to 0.6 (Fig. 10).

430   **3.2 OCO-2 XCO_2 IAV compared to GOSAT XCO_2 IAV**

We carried out comparisons between the global spatiotemporal pattern of XCO_2 IAV between OCO-2 and GOSAT, since GOSAT has data beginning in 2009. The XCO_2 timeseries from OCO-2 provides higher coverage over mid-latitude oceans and tropical rainforests (stippling in Fig. 6, 7). The IAV amplitude of OCO-2 is generally smaller than that of GOSAT worldwide (Fig. 6, 7), which may be due to greater data volume and reduced noise in the OCO-2

435   dataset (Wu et al., 2020). OCO-2 and GOSAT zonal mean IAV timeseries generally share the same feature from 2014 to 2021 (Fig. 4a-d), with an increasing trend during El Niño and decreasing trend during La Niña, however the GOSAT XCO_2 shows a delayed response in the northern midlatitudes, by almost 9 months, to the strong 2015 El Niño compared to the other datasets. Generally, GOSAT IAV timeseries [are] nosier, from month-to-month, compared to those from OCO-2.

440

3.3 XCO_2 IAV compared to surface and TCCON ground-based sites

Given that the small IAV signal (up to 1 ppm over land, and smaller over ocean) is similar in magnitude to noise and systematic bias in OCO-2 soundings (Torres et al., 2019), we corroborate patterns of IAV from OCO-2 with other datasets. The OCO-2 IAV timeseries in broad latitudinal belts share similarities with those of TCCON XCO_2 and

445   MBL surface CO_2 ground-based IAV timeseries, with all timeseries showing similar relationships to MEI. Especially striking is that all timeseries capture the lagged response in the NH midlatitude belt to the strong 2015/16 El Ñino (Fig. 4a-d). Although the patterns are similar, the magnitude of IAV at the MBL sites is almost double the IAV in the OCO-2 XCO_2 timeseries. Given that the atmospheric boundary layer, where surface observations are made, is on average 10% of the total column, this suggests that much IAV in total column observations is present within the free

450   troposphere. For TCCON, the amplitude of IAV is similar to that of OCO-2, since both methods capture total column variations. We note that the zonal IAV timeseries for MBL and TCCON appear to have more high frequency variations than those from OCO-2 (Fig. S10, Fig. S11 & Fig. S12), which likely stems from the fact that the zonal composites are developed from sparse ground-based sites (between 1 and 12 observatories) within each latitude belt, whereas the satellite measures at all longitudes within a belt, though with more limited time resolution. The zonal mean OCO-2

455   observations are correlated with MBL sites within the same latitude band with R between 0.5 and 0.75 (diagonal elements on Fig. 13b). Correlations between zonal TCCON and OCO-2 observations range between 0.15 and 0.55

(Table. S1). The correlations are weakest in the northern tropics band, where TCCON data were unavailable during the strong El Ñino (Fig. 3c). It is noteworthy that OCO-2 zonal averages are more correlated among different latitudes than are MBL or TCCON observations (off-diagonal elements in Fig. 13c, d, e). The greater correlation across latitudes for OCO-2 compared to MBL sites is likely due to the sensitivity of the OCO-2 XCO$_2$ observations to the free troposphere, where meridional transport is more rapid than at the surface. While TCCON data are also sensitive to the free troposphere, we hypothesize that the zonal belt averages for TCCON, constructed from only a few sites, are more affected by noise, both instrumental and geophysical, and thus show lower coherence than the OCO-2 XCO$_2$ averages constructed from the whole latitudinal bands.

We further compared the IAV from OCO-2 XCO$_2$ with TCCON stations at the site level (Fig. 12). Across all sites, the IAV amplitude generally shows good agreement and lies between 0.4 to 1.2 ppm. We note a slight low IAV amplitude in OCO-2 relative to TCCON for all five sites in the Southern Hemisphere which lie below the one-to-one line. Low OCO-2 IAV amplitudes may be due to the fact that a 5x5 ° gridcell encompassing these near-coastal locations includes both land and ocean OCO-2 soundings, and may be due to specific sources of variance from retrieval bias affected by surface type for the OCO-2 (e.g., Fig. 9). It is also worth noting that OCO-2 is looking at a region of 5° by 5° gridcell (or 5° by 10° in higher latitudes) around TCCON sites, so there are different signals affecting the variance between the two types of observations.
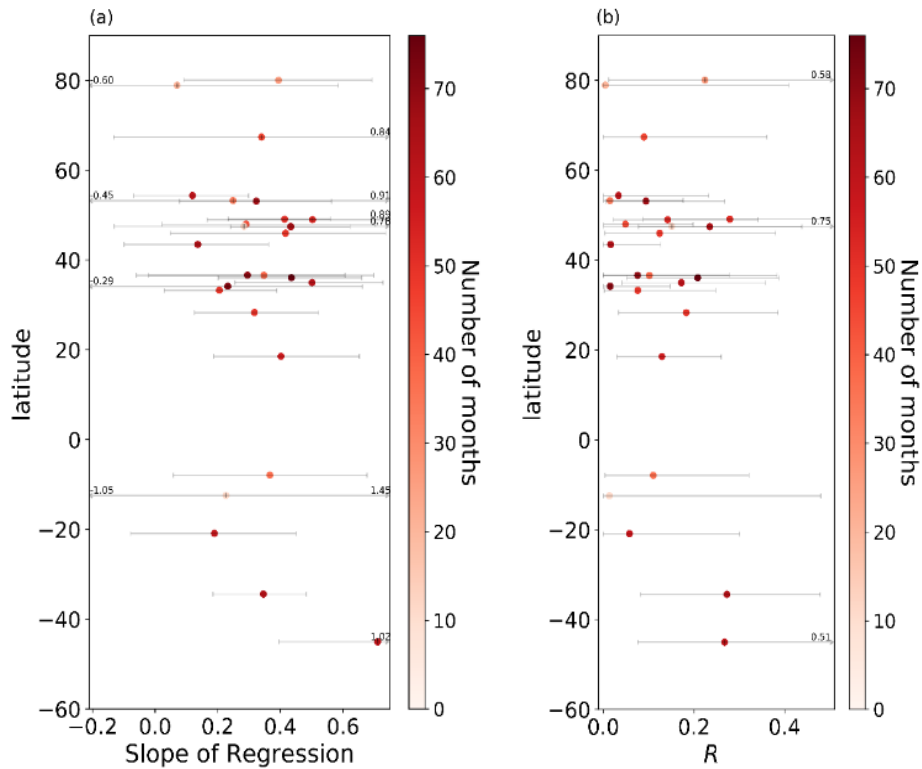
Figure 11. Latitudinal profile of regression Slope (panel a) and correlation coefficient (R, panel b) of OCO-2 versus TCCON XCO$_2$ IAV. The Slope and R values are based on using monthly XCO$_2$ IAV. The error bars result from a Monte Carlo bootstrapping approach . The colours represent the number of months data which used for the regression calculation, given gaps in both the OCO-2 and TCCON datasets.

We derive the regression slopes and Correlation Coefficient R between OCO-2 and monthly averaged TCCON IAV through bootstrapping Linear Regression fitting techniques to investigate the coherence between IAV signals from space-based and in-situ ground-based observations. We compute the linear regression 1000 times, by iteratively resampling the IAV timeseries with replacement, and calculate the 95% significant level for regression slopes based on the histogram of the sample distributions during the bootstrapping (Fig. S13). Despite having similar IAV amplitudes, the IAV timeseries from OCO-2 are only moderately correlated with those from TCCON (Fig. 11). The regression slopes range from 0.1- 0.6 and R values are generally around 0.1 – 0.5, indicating that less than 25% of the IAV in OCO-2 is explained by IAV measured by TCCON. These R values are, as expected, smaller than the zonal averages shown in Fig. 11b, which average some of the site-level noise for TCCON and gridcell-level noise for OCO-2. The detailed XCO_2 IAV timeseries of each site (Fig. S10) for OCO-2 and TCCON show that the IAV timeseries in the NH are more variable, which can partly explain the hemispheric difference in amplitude, slope, and correlation coefficients.
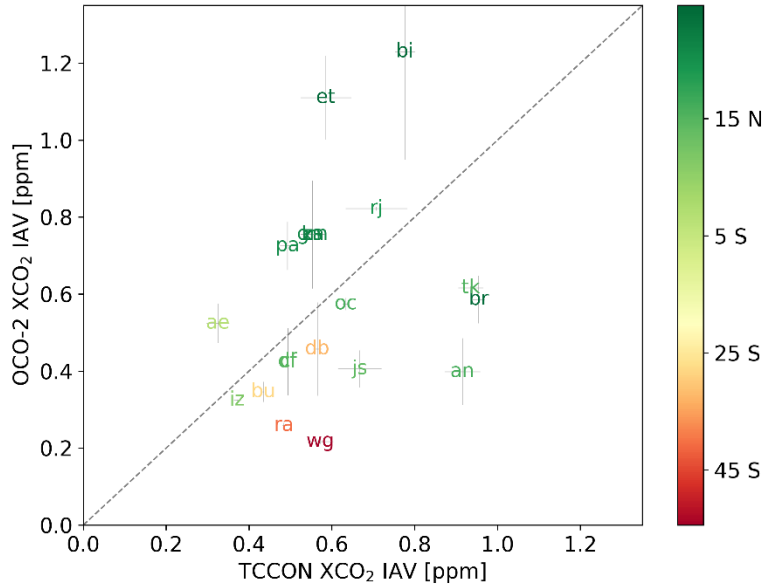
Figure 12. Comparison of OCO-2 and TCCON XCO_2 IAV amplitude at individual sites. Colours reflect site latitudes. The grey dashed line is the one-to-one identity line. The grey solid line is the error bar of the IAV amplitude.

4 Discussion

We use seven years of OCO-2 total column carbon dioxide observations from late 2014 to mid-2021 to illustrate the global temporal-spatial patterns of atmospheric XCO_2 interannual variations. The good agreement among the OCO-2 XCO_2 IAV timeseries, TCCON XCO_2 IAV timeseries and the MBL surface CO_2 IAV timeseries in broad zonal belts improves our confidence that we are able to quantify reasonable IAV timeseries from the satellite record. From the space-based and ground-based detection, we are able to characterize the global response of OCO-2 and TCCON XCO_2 or MBL surface CO_2 IAV to ENSO, and track the CO_2 IAV against the positive/negative phase of ENSO, together with the transport of the signal from South to North (Fig. 4). All datasets show consistent patterns in the response to

the El Ñino periods, although we note that the IAV amplitude is a factor of almost two smaller in the column average mole fraction compared to the boundary layer CO_2, which reflects the fact that IAV variations emerge due to surface fluxes in the lower part of the atmosphere (Olsen & Randerson, 2004), but are efficiently transported into the free troposphere which comprises the bulk of the column. When taken together, the use of surface and column data may allow better separation of transport-driven versus local flux driven variations at the interannual timescale. In the future, as partial column retrievals (e.g., Kulawik et al., 2017) mature, intercomparisons of lowermost tropospheric partial columns may provide a useful bridge between variations in surface MBL observations and total column observations.

Our results, however, underscore the difficulty in detecting IAV signals from remote sensing of XCO_2 -- while northern hemisphere seasonal amplitudes are typically 10 ppm scale (Basu et al., 2011), the magnitude of OCO-2 detected XCO_2 IAV is almost an order of magnitude smaller (less than 0.4 ppm over ocean and about 1ppm over continents). The magnitude of IAV is therefore comparable to other components of the XCO_2 variance budget; for instance, Torres et al. (2019) show random noise in individual OCO-2 soundings of about 0.3 ppm in the southern hemisphere and of about 0.7 ppm in the northern hemisphere, and spatially coherent errors in the retrievals ranging from 0.3 to 0.8 ppm (Torres et al., 2019). Moreover, the uncertainty which originally comes from the varying climatological seasonal cycle, can also reach the level of 0.5ppm (Fig. 3d). Therefore, robust partitioning of IAV from the observed XCO_2 signal at a given location requires a comprehensive variance budget (Mitchell et al., 2023), and efforts to infer interannual variations in fluxes from OCO-2 must take gridcell-level variance into account or leverage zonally averaged data, which is characterized by greater separation between IAV signal and noise.

Our analysis shows that proper spatial averaging of the monthly XCO_2 signal can mitigate the imprint of random noise and systematic effects from weather systems at sub-monthly timescales. Based on sensitivity tests, we recommend averaging low to mid-latitude of XCO_2 (equatorward of 45°) to 5°x5° bins, and 5° latitude x 10° longitude grid cell poleward of 45°, ensuring that each gridcell aggregates at least 5 soundings within a month. At these levels of spatial averaging, the XCO_2 IAV amplitude was comparable to that of the co-located ground based XCO_2 IAV amplitude measured by TCCON (Fig.12). However, the moderate to low correlation between the IAV timeseries from each monitoring platform reveals the discrepancies of the two measurements in sampling, detection or retrieval, suggesting that one or both is still convolving another source of variance with the calculated IAV signal. Based on the good agreement between the two timeseries in broad zonal belts, we expect that random noise in both observations may degrade the comparison.

The smaller coherence in the IAV timeseries in nearby land and ocean gridcells may be due to larger error over land or may reflect that XCO_2 observations over land contain information about heterogeneous local flux IAV. Complete analysis of the variance budget for OCO-2 observations (Mitchell et al., 2023) will elucidate the likely imprint of each process. When using IAV timeseries for flux inference, it will be crucial to account for non-flux imprints such as imprint from atmospheric transport, random errors, systematic errors, and remote geophysical coherence on the timeseries (e.g., Torres et al., 2019; Mitchell et al., 2023), since spurious attribution of IAV will lead to biased fluxes.
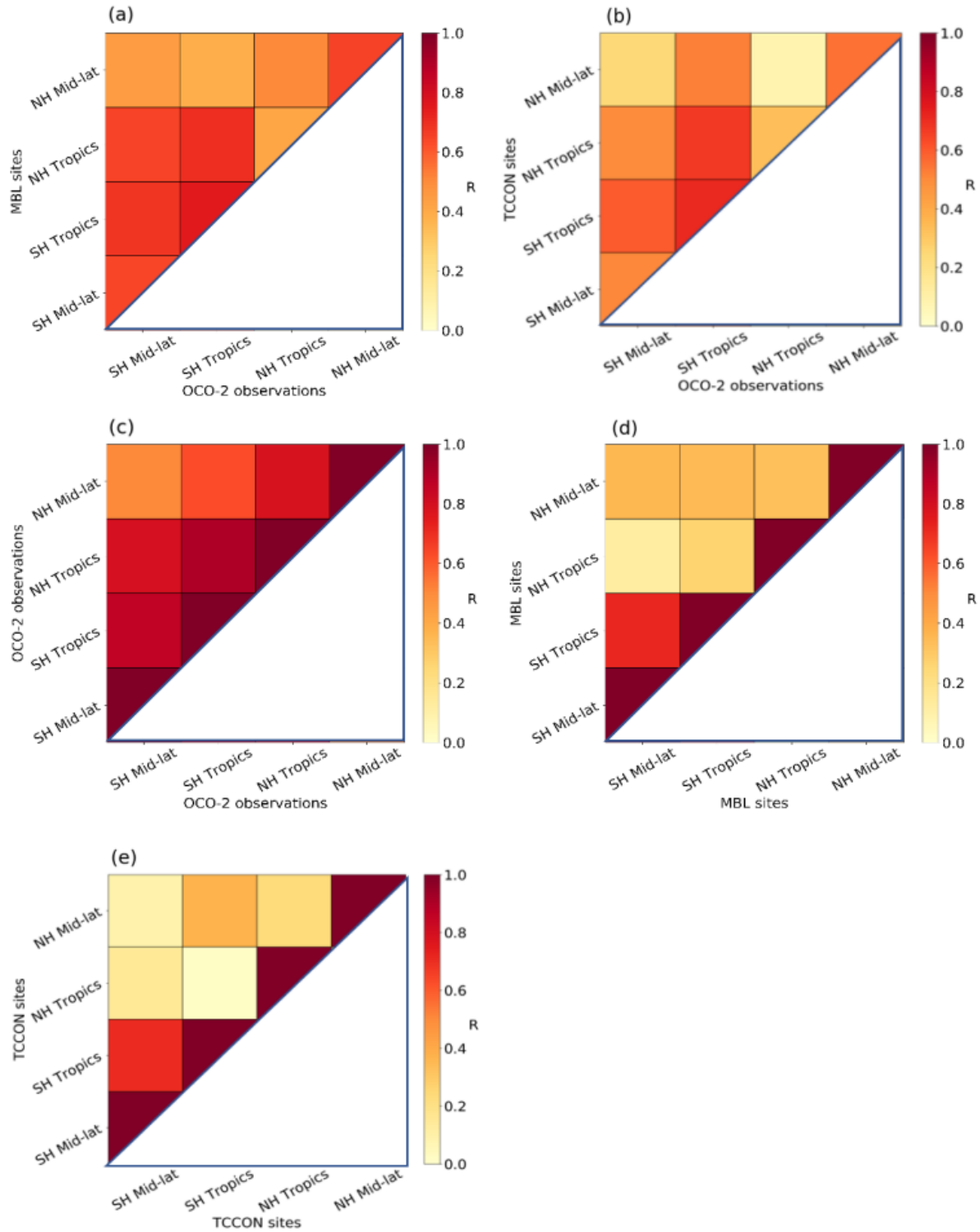
Figure 13. Correlation coefficient (R) between among mean CO$_2$ timeseries using three observing strategies. Panel (a) shows the correlation between zonal mean OCO-2 XCO$_2$ IAV and zonal mean marine boundary layer CO$_2$. Panel (b) shows the correlation between zonal mean XCO$_2$ IAV from OCO-2 and TCCON. Panels (c-e) show the correlation in zonal mean IAV timeseries across four latitude bands for a single observing strategy. Panel (c) shows OCO-2 XCO$_2$, Panel (d) shows MBL CO$_2$ and Panel (e) shows TCCON XCO$_2$. For Panels c-e, the diagonal elements are 1 by construction. Zonal bands include tropical (0°-20°) and NH/SH temperate zone (20°-60°).

5 Conclusions

We examined IAV in OCO-2 data to determine whether the small variations that result from interannual flux variations can be detected in light of other sources of variance in the space-based dataset. Our results show that zonal averages reveal relationships with ENSO that are consistent with those from established ground-based monitoring network. Zonal averages greatly reduce random noise in XCO_2 compared to $5x5^o$ averages. In general, OCO-2 can successfully monitor CO_2 IAV over both land and ocean, contributing important spatial coverage beyond inferences of IAV from existing ground-based networks.

Data availability

The version 10 OCO-2 Level 2 bias-corrected XCO_2 data product is available from Goddard Earth Sciences Data and Information Services Center Archive: https://disc.gsfc.nasa.gov/datasets/OCO2_L2_Lite_FP_10r/summary. TCCON Data is publicly available from the TCCON Data Archive (https://tccondata.org/) hosted by the California Institute of Technology. MBL dry air mole fraction data is available from NOAA Global Monitoring Laboratory Earth System Research Laboratories Archive: https://gml.noaa.gov/ccgg/mbl/data.php.

Author contribution

Formal analysis: Yifan Guan. Writing – original draft preparation: Yifan Guan. Conceptualization: Gretchen Keppel-Aleks. Supervision: Gretchen Keppel-Aleks. Project administration: Gretchen Keppel-Aleks and Scott C. Doney. Writing – review & editing: Gretchen Keppel-Aleks, Scott C. Doney, Christof Petri, Dave Pollard, Debra Wunch, Frank Hase, Hirofumi Ohyama, Isamu Morino, Justus Notholt, Kei Shiomi, Kim Strong, Kivi Rigel, Matthias Buschmann, Nicholas Deutscher, Paul Wennberg, Ralf Sussmann, Voltaire A. Velazco and Yao Té.

Competing interests

The authors declare that they have no conflict of interest.

Acknowledgements

The authors thank the participants of the NASA OCO-2 mission for providing the OCO-2 data product (From GES DISC Archive: https://disc.gsfc.nasa.gov/datasets/OCO2_L2_Lite_FP_10r/summary) used in this study. We thank TCCON partners for providing total column data. We acknowledge NASA support through the OCO Science team and grants 80NSSC18K0897, 80NSSC21K1071, 80NSSC18K0900, and 80NSSC21K1070 to the University of Michigan and University of Virginia. The Paris TCCON site has received funding from Sorbonne Université, the French research center CNRS, the French space agency CNES, and Région Île-de-France. TCCON sites at Tsukuba, Rikubetsu and Burgos are supported in part by the GOSAT series project. Burgos is supported in part by the Energy Development Corp. Philippines, the TCCON site at Reunion Island has been operated by the Royal Belgian Institute for Space Aeronomy with financial support since 2014 by the EU project ICOS-Inwire and the ministerial decree for ICOS (FR/35/IC1 to FR/35/C6) and local activities supported by LACy/UMR8105 and by OSU-R/UMS3365 – Université de La Réunion. The TCCON stations at Garmisch and Zugspitze have been supported by the Helmholtz

Society via the research program "Changing Earth – Sustaining our Future". The Eureka TCCON measurements were made at the Polar Environment Atmospheric Research Laboratory (PEARL) by the Canadian Network for the Detection of Atmospheric Change (CANDAC), primarily supported by the Natural Sciences and Engineering Research Council of Canada, Environment and Climate Change Canada, and the Canadian Space Agency.

References

Ahlström, A., Raupach, M. R., Schurgers, G., Smith, B., Arneth, A., Jung, M., Reichstein, M., Canadell, J. G., Friedlingstein, P., Jain, A. K., Kato, E., Poulter, B., Sitch, S., Stocker, B. D., Viovy, N., Wang, Y. P., Wiltshire, A., Zaehle, S. & Zeng, N. (2015). The dominant role of semi-arid ecosystems in the trend and variability of the land CO_2 sink. *Science*, 348, 895–899. https://doi.org/10.1126/science.aaa1668

Baker, D. F., Bell, E., Davis, K. J., Campbell, J. F., Lin, B., & Dobler, J. (2022). A new exponentially decaying error correlation model for assimilating OCO-2 column-average CO_2 data using a length scale computed from airborne lidar measurements. *Geoscientific Model Development*, *15*(2), 649-668. https://doi.org/10.5194/gmd-15-649-2022

Baker, D. F., Bösch, H., Doney, S. C., O'Brien, D. & Schimel, D. S. (2010). Carbon source/sink information provided by column CO_2 measurements from the Orbiting Carbon Observatory. *Atmospheric Chemistry and Physics*, 10, 4145–4165. https://doi.org/10.5194/acp-10-4145-2010

Baker, D. F., Doney, S. C. & Schimel, D. S. (2006). Variational data assimilation for atmospheric CO_2. *Tellus B: Chemical and Physical Meteorology*, 58:5, 359-365. https://doi.org/10.1111/j.1600-0889.2006.00218.x

Basu, S., Houweling, S., Peters, W., Sweeney, C., Machida, T., Maksyutov, S., Patra, P.K., Saito, R., Chevallier, F., Niwa, Y., Matsueda, H. & Sawa, Y. (2011). The seasonal cycle amplitude of total column CO_2 : Factors behind the model-observation mismatch. *Journal of Geophysical Research: Atmospheres*, 116. https://doi.org/10.1029/2011JD016124

Blumenstock, T., Hase F., Schneider M., Garca O.E. & Sep lveda E. (2017). TCCON data from Izana, Tenerife, Spain, Release GGG2014R1. *TCCON data archive, CaltechDATA*. https://doi.org/10.14291/tccon.ggg2014.izana01.R1

Byrne, B., Liu, J., Lee, M., Baker, I., Bowman, K. W., Deutscher, N. M., Feist, D. G., Griffith, D. W. T., Iraci, L. T., Kiel, M., Kimball, J. S., Miller, C. E., Morino, I., Parazoo, N. C., Petri, C., Roehl, C. M., Sha, M. K., Strong, K., Velazco, V. A., Wennberg, P. O. & Wunch, D. (2020). Improved Constraints on Northern Extratropical CO_2 Fluxes

Obtained by Combining Surface-Based and Space-Based Atmospheric CO_2 Measurements. *Journal of Geophysical Research: Atmospheres*, 125 (15). https://doi.org/10.1029/2019JD032029

Chatterjee, A., Gierach, M.M., Sutton, A.J., Feely, R.A., Crisp, D., Eldering, A., Gunson, M.R., O'Dell, C.W.,
655 Stephens, B.B., & Schimel, D.S. (2017). Influence of El Niño on atmospheric CO_2 over the tropical Pacific Ocean: Findings from NASA's OCO-2 mission. *Science*, 358. https://doi.org/10.1126/science.aam5776

Chevallier, F., Remaud, M., O'Dell, C. W., Baker, D., Peylin, P. & Cozic, A. (2019) Objective 4.1 evaluation of surface-and satellite-driven carbon dioxide atmospheric inversions. *Atmospheric Chemistry and Physics*, 19 14233–
660 51. https://doi.org/10.5194/acp-19-14233-2019

Ciais, P., Sabine, C., Bala, G., Bopp, L., Brovkin, V., Canadell, J., Chhabra, A., DeFries, R., Galloway, J., Heimann, M, Jones, C., LeQuéré, C., Myneni, R. B., Piao, S., & Thorton, P. (2013). Carbon and Other Biogeochemical Cycles, in Climate Change 2013: edited by Stocker et al., The physical science basis. Contribution of working group I to the
665 fifth assessment report of the intergovernmental panel on climate change (pp. 1–106).

Crisp, D., Bosch, H., Brown, L., Castano, R., Christi, M., Connor, B., Frankenberg, C., McDuffie, J., Miller, C. E., Natraj, V., O'Dell, C., O'Brien, D., Polonsky, I., Oyafuso, F., Thompson, D., Toon, G. & Spurr, R. (2010). OCO (Orbiting Carbon Observatory)-2 Level 2 Full Physics Retrieval Algorithm Theoretical Basis, Tech. Rep. OCO D-
670 65488, NASA Jet Propulsion Laboratory, California Institute of Technology, Pasadena, CA, version 1.0 Rev 4, http://disc.sci.gsfc.nasa.gov/acdisc/ documentation/OCO-2 L2 FP ATBD v1 rev4 Nov10.pdf, (last access: January 2012).

Crisp, D., Fisher, B. M., O'Dell, C., Frankenberg, C., Basilio, R., Bösch, H., Brown, L. R., Castano, R., Connor, B.,
675 Deutscher, N. M., Eldering, A., Griffith, D., Gunson, M., Kuze, A., Mandrake, L., McDuffie, J., Messerschmidt, J., Miller, C. E., Morino, I., Natraj, V., Notholt, J., O'Brien, D. M., Oyafuso, F., Polonsky, I., Robinson, J., Salawitch, R., Sherlock, V., Smyth, M., Suto, H., Taylor, T. E., Thompson, D. R., Wennberg, P. O., Wunch, D. & Yung, Y. L. (2012). The ACOS CO_2 retrieval algorithm – Part II: Global XCO_2 data characterization. *Atmospheric Measurement Techniques*, 5, 687– 707. https://doi.org/10.5194/amt-5-687-2012.
680
Crisp, D., Pollock, H. R., Rosenberg, R., Chapsky, L., Lee, R. A. M., Oyafuso, F. A., Frankenberg, C., O'Dell, C. W., Bruegge, C. J., Doran, G. B., Eldering, A., Fisher, B. M., Fu, D., Gunson, M. R., Mandrake, L., Osterman, G. B., Schwandner, F. M., Sun, K., Taylor, T. E., Wennberg, P. O. & Wunch, D. (2017). The on-orbit performance of the Orbiting Carbon Observatory-2 (OCO-2) instrument and its radiometrically calibrated products. *Atmospheric*
685 *Measurement Techniques*, 10, 59–81. https://doi.org/10.5194/amt-10-59-2017.

Cogan A.J., Boesch H., Parker R. J., Feng L., Palmer P. I., Blavier J.-F. L., Deutscher N. M., Macatangay R., Notholt J., Roehl C., Warneke T., Wunch D. (2012). Atmospheric carbon dioxide retrieved from the Greenhouse gases Observing SATellite (GOSAT): Comparison with ground-based TCCON observations and GEOS-Chem model calculations, *Journal of Geophysical Research*, 117, D21301, doi:10.1029/2012JD018087.

Connor, B., Bösch, H., McDuffie, J., Taylor, T., Fu, D., Frankenberg, C., O'Dell, C., Payne, V. H., Gunson, M., Pollock, R., Hobbs, J., Oyafuso, F. & Jiang, Y. (2016). Quantification of uncertainties in OCO-2 measurements of XCO_2: simulations and linear error analysis. *Atmospheric Measurement Techniques*, 9, 5227–5238. https://doi.org/10.5194/amt-9-5227-2016

Conway, T.J., Tans, P.P., Waterman, L.S., Thoning, K.W., Kitzis, D.R., Masarie, K.A. & Zhang, N. (1994). Evidence for interannual variability of the carbon cycle from the NOAA/CMDL global air sampling network. *Journal of Geophysical Research: Atmospheres*, 99, 22831-22855. https://10.1029/94JD01951

Cox, P.M., Pearson, D., Booth, B.B., Friedlingstein, P., Huntingford, C., Jones, C.D. & Luke, C.M.(2013). Sensitivity of tropical carbon to climate change constrained by carbon dioxide variability. *Nature*, 494(7437):341-4. https://doi.org/10.1038/nature11882.

Crowther, T. W., Glick, H. B., Covey, K. R., Bettigole, C., Maynard, D. S., Thomas, S. M., Smith, J. R., Hintler, G., Duguid, M. C., Amatulli, G., Tuanmu, M.-N., Jetz, W., Salas, C., Stam, C., Piotto, D., Tavani, R., Green, S., Bruce, G., Williams, S. J., Wiser, S. K., Huber, M. O., Hengeveld, G. M., Nabuurs, G.-J., Tikhonova, E., Borchardt, P., Li, C.-F., Powrie, L. W., Fischer, M., Hemp, A., Homeier, J., Cho, P., Vibrans, A. C., Umunay, P. M., Piao, S. L., Rowe, C. W., Ashton, M. S., Crane, P. R. & Bradford, M. A. (2015). Mapping tree density at a global scale. *Nature*, 525**,** 201–205. https://doi.org/10.1038/nature14967

De Maziere, M., Sha, M. K., Desmet, F., Hermans, C., Scolas, F., Kumps, N., Metzger, J.-M., Duflot, V. & Cammas, J.-P. (2017). TCCON data from Reunion Island (La Reunion), France, Release GGG2014R0. *TCCON data archive, CaltechDATA*. https://doi.org/10.14291/tccon.ggg2014.reunion01.R0/1149288

Deutscher, N., Notholt, J., Messerschmidt, J., Weinzierl, C., Warneke, T., Petri, C., Grupe, P. & Katrynski, K.(2017). TCCON data from Bialystok, Poland, Release GGG2014R1. *TCCON data archive, CaltechDATA*. http://doi.org/10.14291/tccon.ggg2014.bialystok01.R1/1183984

Dlugokencky, E. J., Lang, P. M., Mund, J. W., Crotwell, A. M., Crotwell, M. J., & Thoning, K. W. (2016). Atmospheric carbon dioxide dry air mole fractions from the NOAA ESRL carbon cycle cooperative global air sampling network, 1968–2015, version 2016- 08-30, NOAA, available at: ftp://aftp.cmdl.noaa.gov/data/trace_gases/co2/flask/surface/

725   Doney, S. C., Lima, I., Feely, R. A., Glover, D. M., Lindsay, K., Mahowald, N., Moore, J. K., & Wanninkhof, R. (2009). Mechanisms governing interannual variability in upper-ocean inorganic car-bon system and air–sea CO_2 fluxes: Physical climate and atmospheric dust, Deep-Sea Res. Pt. II, 56, 640–655. https://doi.org/10.1016/j.dsr2.2008.12.006$

730   Feely, R.A, Wanninkhof, R., Takahashi, T. & Tans, P. (1999). Influence of El Niño on the equatorial Pacific contribution to atmospheric CO_2 accumulation. *Nature*. 398, 597–601. https://doi.org/10.1038/19273

Feely, R. A., Boutin, J., Cosca, C., Dandonneau, Y., Etcheto, J., Inoue, H. Y., Ishill, M., Le, Quere C., Mackey, D. J., McPhaden, M., Metzl, N., Poisson, A., & Wanninkhof, R. (2002). Seasonal and interannual variability of CO_2 in the
735   equatorial Pacific. *Deep-Sea Research Part II: Topical Studies in Oceanography*, 49(13-14), 2443-2469. https://doi.org/10.1016/S0967-0645(02)00044-9

Feist, D. G., Arnold, S. G., John, N. & Geibel, M. C.(2017). TCCON data from Ascension Island, Saint Helena, Ascension and Tristan da Cunha, Release GGG2014R0. *TCCON data archive, CaltechDATA*.
740   http://doi.org/10.14291/tccon.ggg2014.ascension01.R0/1149285

Francey, R. J., Tans, P. P., Allison, C. E., Enting, I. G., White, J. W. C. & Trolier, M.(1995). Changes in Oceanic and Terrestrial Carbon Uptake since 1982. *Nature*, 373, 326–330. https://doi.org/10.1038/373326a0

745   Friedlingstein, P., Jones, M. W., O'Sullivan, M., Andrew, R. M., Hauck, J., Peters, G. P., et al. (2019). Global carbon budget 2019. Earth System Science Data, 11(4), 1783–1838. https://essd.copernicus.org/articles/11/1783/2019/
IPCC, 2021: Climate Change 2021: The Physical Science Basis. Contribution of Working Group I to the Sixth Assessment Report of the Intergovernmental Panel on Climate Change [Masson-Delmotte, V., Zhai P., Pirani A., Connors S.L., Péan C., Berger S., Caud N., Chen Y., Goldfarb L., Gomis M.I, Huang M., Leitzell K., Lonnoy E.,
750   Matthews J.B.R., Maycock T.K., Waterfield T., Yelekçi O., Yu R., and Zhou B. (eds.)]. Cambridge University Press, Cambridge, United Kingdom and New York, NY, USA, In press. https://doi.org/10.1017/9781009157896.

Goo, T.-Y., Oh, Y.-S. & Velazco, V. A.. (2017). TCCON data from Anmeyondo, South Korea, Release GGG2014R0. *TCCON data archive, CaltechDATA*.
755   https://doi.org/10.14291/tccon.ggg2014.anmeyondo01.R0/1149284

Griffith, D. W. T., Deutscher, N., Velazco, V. A., Wennberg, P. O., Yavin, Y., Keppel Aleks, G., Washenfelder, R., Toon, G. C., Blavier, J.-F., Murphy, C., Jones, N., Kettlewell, G., Connor, B., Macatangay, R., Roehl, C., Ryczek, M., Glowacki, J., Culgan, T. & Bryant, G.. (2017). TCCON data from Darwin, Australia, Release GGG2014R0. *TCCON*
760   *data archive, CaltechDATA*. http://doi.org/10.14291/tccon.ggg2014.darwin01.R0/1149290

Griffith, D. W. T., Velazco, V. A., Deutscher, N., Murphy, C., Jones, N., Wilson, S., Macatangay, R., Kettlewell, G., Buchholz, R. R. & Riggenbach, M. (2017). TCCON data from Wollongong, Australia, Release GGG2014R0. *TCCON data archive, CaltechDATA*. https://doi.org/10.14291/tccon.ggg2014.wollongong01.R0/1149291

765

Gruber, N., Keeling, C. D. & Bates, N. R. (2002). Interannual variability in the North Atlantic Ocean carbon sink. *Science* 298(5602): 2374-2378. https://doi.org/10.1126/science.1077077

Gurney, K.R., Baker, D., Rayner, P. & Denning, S. (2008). Interannual variations in continental-scale net carbon 770 exchange and sensitivity to observing networks estimated from atmospheric CO_2 inversions for the period 1980 to 2005. Global Biogeochemical Cycles, 22, GB3025. https://doi.org/10.1029/2007GB003082.

Hase, F., Blumenstock, T., Dohe, S., Gro, J. & Kiel, M. (2017). TCCON data from Karlsruhe, Germany, Release GGG2014R1. *TCCON data archive, CaltechDATA*.https://doi.org/10.14291/tccon.ggg2014.karlsruhe01.R1/1182416

775

Humphrey, V., Zscheischler, J., Ciais, P., Gudmundsson, L., Sitch, S. & Seneviratne, S. I. (2018). Sensitivity of atmospheric CO_2 growth rate to observed changes in terrestrial water storage. *Nature* 560, 628–631. https://doi.org/10.1038/s41586-018-0424-4

780 Kivi, R., Heikkinen, P. & Kyro, E. (2017). TCCON data from Sodankyla, Finland, Release GGG2014R0. *TCCON data archive, CaltechDATA*. https://doi.org/10.14291/tccon.ggg2014.sodankyla01.R0/1149280

Iraci, L., Podolske, J., Hillyard, P., Roehl, C., Wennberg, P. O., Blavier, J.-F., Landeros, J., Allen, N., Wunch, D., Zavaleta, J., Quigley, E., Osterman, G., Albertson, R., Dunwoody, K. & Boyden, H.. (2017). TCCON data from 785 Armstrong Flight Research Center, Edwards, CA, USA, Release GGG2014R1. *TCCON data archive, CaltechDATA*. https://doi.org/10.14291/tccon.ggg2014.edwards01.R1/1255068

Jones, C.D., Collins, M., Cox, P.M. & Spall, S.A. (2001). The carbon cycle response to ENSO: a coupled climate-carbon cycle model study. *Journal of Climate*, 14, 4113–4129. https://doi.org/10.1175/1520-790 0442(2001)014<4113:TCCRTE>2.0.CO;2

Karion, A., Sweeney, C., Tans, P. & Newberger, T. (2010). AirCore: An Innovative Atmospheric Sampling System. *Journal of Atmospheric and Oceanic Technology*, 27. 1839-1853. https://doi.org/10.1175/2010JTECHA1448.1

795 Keenan, T.F. & Williams, C.A. (2018). The Terrestrial Carbon Sink. *Annual Review of Environment and Resources*, 2018 43:1, 219-243. https://doi.org/10.1146/annurev-environ-102017-030204

Keppel-Aleks, G., Wennberg, P. O., Washenfelder, R. A., Wunch, D., Schneider, T., Toon, G. C., Andres, R. J., Blavier, J.-F., Connor, B., Davis, K. J., Desai, A. R., Messerschmidt, J., Notholt, J., Roehl, C. M., Sherlock, V., Stephens, B. B., Vay, S. A., & Wofsy, S. C. (2012). The imprint of surface fluxes and transport on variations in total column carbon dioxide. *Biogeosciences*, 9, 875–891. https://doi.org/10.5194/bg-9-875-2012

Keppel-Aleks, G., Wolf, A. S., Mu, M., Doney, S. C., Morton, D. C., Kasibhatla, P. S., Miller, J. B., Dlugokencky, E. J. & Randerson, J. T. (2014). Separating the influence of temperature, drought, and fire on interannual variability in atmospheric CO_2. *Global Biogeochemica Cycles*, 28 1295–310. https://doi.org/10.1002/2014GB004890

Kivi, R. and Heikkinen, P.: Fourier transform spectrometer measurements of column CO_2 at Sodankylä, Finland, Geosci. Instrum. Method. Data Syst., 5, 271–279, https://doi.org/10.5194/gi-5-271-2016, 2016.

Kobayashi, S., Ota, Y., Harada, Y., Ebita, A., Moriya, M., Onoda, H., Onogi, K., Kamahori, H., Kobayashi, C., Endo, H., Miyaoka, K. & Takahashi, K.(2015). The JRA-55 Reanalysis: general specifications and basic characteristics. *Journal of the Meteorological Society of Japan*, 93, 5-48. https://doi.org/10.2151/jmsj.2015-001

Kulawik, S., Wunch, D., O'Dell, C., Frankenberg, C., Reuter, M., Oda, T., Chevallier, F., Sherlock, V., Buchwitz, M., Osterman, G., Miller, C. E., Wennberg, P. O., Griffith, D., Morino, I., Dubey, M. K., Deutscher, N. M., Notholt, J., Hase, F., Warneke, T., Sussmann, R., Robinson, J., Strong, K., Schneider, M., De Mazière, M., Shiomi, K., Feist, D. G., Iraci, L. T., and Wolf, J. (2016). Consistent evaluation of ACOS-GOSAT, BESD-SCIAMACHY, CarbonTracker, and MACC through comparisons to TCCON, *Atmospheric Measuring Techniques*, 9, 683–709, https://doi.org/10.5194/amt-9-683-2016

Landschützer, P., Gruber, N., Bakker, D. C. E., Schuster, U., Nakaoka, S., Payne, M. R., Sasse, T. P. & Zeng, J. (2013). A neural network-based estimate of the seasonal to inter-annual variability of the Atlantic Ocean carbon sink. *Biogeosciences*, 10, 7793–7815. https://doi.org/10.5194/bg-10-7793-2013

Landschützer, P., Gruber, N. & Bakker, D. C. E. (2016). Decadal variations and trends of the global ocean carbon sink. *Global Biogeochemical Cycles*, 30, 1396– 1417. https://doi.org/10.1002/2015GB005359

Le Quéré, C., Aumont, O., Bopp, L., Bousquet, P., Ciais, P., Francey, R., Heimann, M., Keeling, C.D., Keeling, R.F., Khesghi, H., Peylin, P., Piper, S.C., Prentice, I.C. & Rayner, P.J. (2003). Two decades of ocean CO_2 sink and variability. Tellus B : *Chemical and Physical Meteorology*, 55B, p. 649-656. International Carbon Dioxide Conference, 6., Sendaï (JPN), 2011/10/01-05.

Le Quere, C., Raupach, M. R., Canadell, J. G., Marland, G., Bopp, L., Ciais, P., Conway, T. J., Doney, S. C., Feely, R. A., Foster, P., Friedlingstein, P., Gurney, K., Houghton, R. A., House, J. I., Huntingford, C., Levy, P. E., Lomas,

835   M. R., Majkut, J., Metzl, N., Ometto, J. P., Peters, G. P., Prentice, I. C., Randerson, J. T., Running, S. W., Sarmiento, J. L., Schuster, U., Sitch, S., Takahashi, T., Viovy, N., van der Werf, G. R. & Woodward, F. I. (2009). Trends in the sources and sinks of carbon dioxide. *Nature Geoscience*, 2(12), 831-836. https://doi.org/10.1038/ngeo689.

Nassar, R., Jones, D. B. A., Kulawik, S. S., Worden, J. R., Bowman, K. W., Andres, R. J., Suntharalingam, P., Chen,
840   J. M., Brenninkmeijer, C. A. M., Schuck, T. J., Conway, T. J., & Worthy, D. E. (2011). Inverse modeling of CO_2 sources and sinks using satellite observations of CO_2 from TES and surface flask measurements, *Atmospheric Chemistry and Physics*, 11, 6029–6047. https://doi.org/10.5194/acp-11-6029-2011.

Wu, L., Aan De Brugh, J., Meijer, Y., Sierk, B., Hasekamp, O., Butz, A., & Landgraf, J.(2020). XCO_2 observations
845   using satellite measurements with moderate spectral resolution: investigation using GOSAT and OCO-2 measurements, *Atmospheric Measurement Techniques*, 13, 713–729, https://doi.org/10.5194/amt-13-713-2020.

Liu J., Bowman, K. W., Schimel, D. S., Parazoo, N. C., Jiang, Z., Lee, M., Bloom, A. A., Wunch, D., Frankenberg, C., Sun, Y., O'Dell, C. W., Gurney, K. R., Menemenlis, D., Gierach, M., Crisp, D. & Eldering, A.(2017). Contrasting
850   carbon cycle responses of the tropical continents to the 2015-2016 El Niño. *Science*. https://doi.org/10.1126/science.aam5690.

Marcolla, B., Rödenbeck, C., & Cescatti, A. (2017). Patterns and controls of inter-annual variability in the terrestrial carbon budget. *Biogeosciences*, 14, 3815–3829. https://doi.org/10.5194/bg-14-3815-2017
855

Masarie, K.A. & Tans, P.P. (1995). Extension and Integration of Atmospheric Carbon Dioxide Data into a Globally Consistent Measurement Record. *Journal of Geophysical Research*, 100(D6), 11593– 11610. https://doi.org/10.1029/95JD00859

860   McKinley, G.A., Rödenbeck, C., Gloor, M., Houweling, S. & Heimann, M. (2004). Pacific dominance to global air-sea CO_2 flux variability: A novel atmospheric inversion agrees with ocean models. *Geophysical Research Letters*, 31, L22308. https://doi.org/10.1029/2004GL021069.

Miller, S. M., Michalak, A. M., Yadav, V. & Tadić, J. M. (2018). Characterizing biospheric carbon balance using CO_2
865   observations from the OCO-2 satellite. *Atmospheric Chemistry and Physics*, 18, 6785–6799. https://doi.org/10.5194/acp-18-6785-2018

Mitchell, K. A., Doney S. C. & Keppel-Aleks G. (2023). Characterizing average seasonal, synoptic, and finer variability in Orbiting Carbon Observatory-2 XCO_2 across North America and adjacent ocean basins, *Journal of*
870   *Geophysical Research: Atmospheres*, 128, e2022JD036696. https://doi.org/10.1029/2022JD036696.

Morino, I., Matsuzaki, T. & Shishime, A. (2017). TCCON data from Tsukuba, Ibaraki, Japan, 125HR, Release GGG2014R1. *TCCON data archive, CaltechDATA*. http://doi.org/10.14291/tccon.ggg2014.tsukuba02.R1/1241486

875   Morino, I., Velazco, V. A., Hori, A., Uchino, O., & Griffith, D. W. T. (2018). TCCON data from Burgos, Ilocos Norte (PH), Release GGG2014.R0. *TCCON data archive, CaltechDATA*. https://doi.org/10.14291/TCCON.GGG2014.BURGOS01.R0

Morino, I., Yokozeki, N., Matzuzaki, T. & Shishime, A. (2017). TCCON data from Rikubetsu, Hokkaido, Japan, 880   Release GGG2014R1. *TCCON data archive, CaltechDATA*. https://doi.org/10.14291/tccon.ggg2014.rikubetsu01.R1/1242265

Mudelsee, M. (2014). Climate Time Series Analysis: Classical Statistical and Bootstrap Methods Second edition. Springer, Cham Heidelberg New York Dordrecht London. https://doi.org/10.1007/978-3-319-04450-7

885

Nassar, R., Jones, D. B. A., Suntharalingam, P., Chen, J. M., Andres, R. J., Wecht, K. J., Yantosca, R. M., Kulawik, S. S., Bowman, K. W., Worden, J. R., Machida, T., & Matsueda, H. (2010). Modeling global atmospheric CO_2 with improved emission inventories and CO_2 production from the oxidation of other carbon species. *Geoscientific Model Development*, 3, 689–716. https://doi.org/10.5194/gmd-3-689-2010

890

Nevison, C. D., Mahowald, N. M., Doney, S. C., Lima, I. D., van der Werf, G. R., Randerson, J. T., Baker, D. F., Kasibhatla, P. & McKinley, G. A. (2008). Contribution of ocean, fossil fuel, land biosphere, and biomass burning carbon fluxes to seasonal and interannual variability in atmospheric CO_2. *Journal of Geophysical Research: Biogeosciences*, 113, G0101. https://doi.org/10.1029/2007JG000408

895

Notholt, J., Petri C., Warneke, T., Deutscher, N., Buschmann, M., Weinzierl, C., Macatangay, R. & Grupe, P. (2017). TCCON data from Bremen, Germany, Release GGG2014R0. *TCCON data archive, CaltechDATA*. https://doi.org/10.14291/tccon.ggg2014.bremen01.R0/1149275

900   Notholt, J., Warneke, T., Petri, C., Deutscher, N. M., Weinzierl, C., Palm, M., & Buschmann, M. (2019). TCCON data from Ny Ålesund, Spitsbergen (NO), Release GGG2014.R1. *TCCON data archive, CaltechDATA*. https://doi.org/10.14291/TCCON.GGG2014.NYALESUND01.R1

O'Dell, C. W., Connor, B., Bösch, H., O'Brien, D., Frankenberg, C., Castano, R., Christi, M., Eldering, D., Fisher, B., 905   Gunson, M., McDuffie, J., Miller, C. E., Natraj, V., Oyafuso, F., Polonsky, I., Smyth, M., Taylor, T., Toon, G. C., Wennberg, P. O. & Wunch, D. (2012). The ACOS CO_2 retrieval algorithm—Part 1: Description and validation against synthetic observations. *Atmospheric Measurement Techniques*, 5(1), 99–121. https://doi.org/10.5194/ amt-5-99-2012

910 O'Dell, C. W., Eldering, A., Wennberg, P. O., Crisp, D., Gunson, M. R., Fisher, B., Frankenberg, C., Kiel, M., Lindqvist, H., Mandrake, L., Merrelli, A., Natraj, V., Nelson, R. R., Osterman, G. B., Payne, V. H., Taylor, T. E., Wunch, D., Drouin, B. J., Oyafuso, F., Chang, A., McDuffie, J., Smyth, M., Baker, D. F., Basu, S., Chevallier, F., Crowell, S. M. R., Feng, L., Palmer, P. I., Dubey, M., García, O. E., Griffith, D. W. T., Hase, F., Iraci, L. T., Kivi, R., Morino, I., Notholt, J., Ohyama, H., Petri, C., Roehl, C. M., Sha, M. K., Strong, K., Sussmann, R., Te, Y., Uchino, O.,
915 and Velazco, V. A.(2018). Improved retrievals of carbon dioxide from Orbiting Carbon Observatory-2 with the version 8 ACOS algorithm. *Atmospheric Measurement Techniques*, 11, 1–57. https://doi.org/10.5194/amt-2018-257

Olsen, S. C. & Randerson , J. T. (2004). Differences between surface and column atmospheric CO_2 and implications for carbon cycle research. *Journal of Geophysical Research*, 109, D02301. https://doi.org/10.1029/2003JD003968
920

Patra, P.k., Maksyutov, S., Ishizawa, M., Nakazawa, T., Takahashi, T. & Ukita, J. (2005). Interannual and decadal changes in the sea–air CO_2 flux from atmospheric CO_2 inverse modeling. *Global Biogeochemical Cycles*, 19, GB4013. https://doi.org/10.1029/2004GB002257

925 Peylin, P., P. Bousquet, C. LeQuere, S. Sitch, P. Friedlingstein, G.A. McKinley, N. Gruber, P. Rayner & P. Ciais (2005). Multiple constraints of regional CO_2 flux variations over land and oceans, *Global Biogeochemical Cycles*, 19, GB1011. https://doi.org/10/1029/2003GB002214

Piao S., Sitch S., Ciais P., Friedlingstein P., Peylin P., Wang X., Ahlström A., Anav A., Canadell J.G., Cong N.,
930 Huntingford C., Jung M., Levis S., Levy P.E., Li J., Lin X., Lomas M.R., Lu M., Luo Y., Ma Y., Myneni R.B., Poulter B., Sun Z., Wang T., Viovy N., Zaehle S. & Zeng N. (2013). Evaluation of terrestrial carbon cycle models for their response to climate variability and to CO_2 trends. *Global Change Biology*, 19: 2117-2132. https://doi.org/10.1111/gcb.12187

935 Piao S., Wang X., Wang K., Li X., Bastos A., Canadell J. G., Ciais P., Friedlingstein P. & Sitch S. (2020). Interannual variation of terrestrial carbon cycle: issues and perspectives. *Global Change Biology*, 26,300–18. https://doi.org/10.1111/gcb.14884

Poulter, B., Frank, D., Ciais, P., Myneni, R.B., Andela, N., Bi, J., Broquet, G., Canadell, J.G., Chevallier, F., Liu,
940 Y.Y., Running, S.W., Sitch, S. & Van Der Werf G.R. (2014). Contribution of semi-arid ecosystems to interannual variability of the global carbon cycle. *Nature*, 509, 600–603. https://doi.org/10.1038/nature13376

Prentice, IC., Farquhar, GD., Fasham, MJR., Goulden, ML., Heimann, M., Jaramillo, VJ., Kheshgi, HS., Le Quéré, C., Scholes, RJ., & Wallace, DWR. (2001). The carbon cycle and atmospheric carbon dioxide. In J. T. Houghton, Y.

945   Ding, D. J. Griggs, M. Noguer, P. J. V. D. Linden, X. Dai, K. Maskell, & C. A. Johnson (Eds.). *Climate Change 2001: The Scientific Basis* (pp. 183 - 237). Cambridge University Press.

Randerson, J.T. (2013). Global warming and tropical carbon. *Nature* 494, 319–320, https://doi.org/10.1038/nature11949

950

Rödenbeck, C., Bakker, D. C. E., Gruber, N., Iida, Y., Jacobson, A. R., Jones, S., Landschützer, P., Metzl, N., Nakaoka, S., Olsen, A., Park, G.-H., Peylin, P., Rodgers, K. B., Sasse, T. P., Schuster, U., Shutler, J. D., Valsala, V., Wanninkhof, R., & Zeng, J. (2015). Data-based estimates of the ocean carbon sink variability – first results of the Surface Ocean pCO$_2$ Mapping intercomparison (SOCOM). *Biogeosciences*, 12, 7251–7278.
955   https://doi.org/10.5194/bg-12-7251-2015

Rödenbeck, C., Bakker, D. C. E., Metzl, N., Olsen, A., Sabine, C., Cassar, N., Reum, F., Keeling, R. F., & Heimann, M. (2014). Interannual sea-air CO$_2$ flux variability from an observation driven ocean mixed-layer scheme. *Biogeosciences*, 11, 4599– 4613. https://doi.org/10.5194/bg-11-4599-2014

960

Schwalm, C. R., Williams, C. A., Schaefer, K., Baker, I., Collatz, G. J. & Rödenbeck, C. (2011). Does terrestrial drought explain global CO$_2$ flux anomalies induced by El Niño? *Biogeosciences*, 8, 2493–2506. https://doi.org/10.5194/bg-8-2493-2011

965   Shiomi, K., Kawakami, S., Ohyama, H., Arai K., Okumura H., Taura C., Fukamachi T. & Sakashita M. (2017). TCCON data from Saga, Japan, Release GGG2014R0. *TCCON data archive, CaltechDATA*. https://doi.org/10.14291/tccon.ggg2014.saga01.R0/1149283

Sherlock, V., Connor B., Robinson J., Shiona H., Smale D., Pollard D. (2017). TCCON data from Lauder, New
970   Zealand, 125HR, Release GGG2014R0. *TCCON data archive, CaltechDATA*.
       https://doi.org/10.14291/tccon.ggg2014.lauder02.R0/1149298

Spring, A., Ilyina, T. & Marotzke, J. (2020). Inherent uncertainty disguises attribution of reduced atmospheric CO$_2$ growth to CO$_2$ emission reductions for up to a decade. *Environmental Research Letters*, 15, 114058.
975   https://doi.org/10.1088/1748-9326/abc443

Strong, K., Mendonca J., Weaver D., Fogal P., Drummond J.R., Batchelor R., Lindenmaier R. (2017). TCCON data from Eureka, Canada, Release GGG2014R2. *TCCON data archive, CaltechDATA*. http://doi.org/10.14291/tccon.ggg2014.eureka01.R2

980

Sussmann, R. & Rettinger. M. (2017). TCCON data from Garmisch, Germany, Release GGG2014R0. *TCCON data archive, CaltechDATA*. https://doi.org/10.14291/tccon.ggg2014.garmisch01.R0/1149299

Sussmann, R. & Rettinger, M. (2018). TCCON data from Zugspitze (DE), Release GGG2014.R1. *TCCON data archive, CaltechDATA*. https://doi.org/10.14291/TCCON.GGG2014.ZUGSPITZE01.R1

Sussmann, R., and Rettinger, M. (2020): Can We Measure a COVID-19-Related Slowdown in Atmospheric CO_2 Growth? Sensitivity of Total Carbon Column Observations, Remote Sens., 12, 2387, https://doi.org/10.3390/rs12152387

Takahashi, T., Sutherland, S.C., Feely, R.A. & Cosca, C.E. (2003). Decadal variation of the surface water PCO_2 in the western and central equatorial Pacific. *Science (New York, N.Y.),* 302(5646):852-6. https://doi.org/10.1126/science.1088570

Té, Y., Jeseck, P., and Janssen, C.: TCCON data from Paris (FR), Release GGG2014.R0, https://doi.org/10.14291/tccon.ggg2014.paris01.r0/1149279, 2014.

Thoning, K. W., Tans, P. P., & Komhyr, W. D. (1989). Atmospheric carbon dioxide at Mauna Loa Observatory: 2. Analysis of the NOAA GMCC data, 1974–1985. *Journal of Geophysical Research*, 94(D6), 8549– 8565. https://doi.org/10.1029/JD094iD06p08549

Timmermann, A., An, S.I., Kug, J.S., Jin, F.F., Cai, W., Capotondi A., Cobb, K.M., Lengaigne, M., McPhaden, M.J., Stuecker, M.F., Stein, K., Wittenberg, A.T., Yun, K.S., Bayr, T., Chen, H.C., Chikamoto, Y., Dewitte, B., Dommenget, D., Grothe, P., Guilyardi, E., Ham, Y.G., Hayashi, M., Ineson, S., Kang, D., Kim, S., Kim, W., Lee, J.Y., Li, T., Luo, J.J., McGregor, S., Planton, Y., Power, S., Rashid, H., Ren, H.L., Santoso, A., Takahashi, K., Todd, A., Wang, G., Wang, G., Xie, R., Yang, W.H., Yeh, S.W., Yoon, J., Zeller, E. & Zhang, X. (2018). El Niño–Southern Oscillation complexity. *Nature* 559, 535–545. https://doi.org/10.1038/s41586-018-0252-6

Wang, J., Zeng, N. , Liu, Y.& Bao, Q. (2014). To what extent can interannual CO_2 variability constrain carbon cycle sensitivity to climate change in CMIP5 Earth system models? *Geophysical Research Letters*, 41, 3535–3544. https://doi.org/10.1002/2014GL060004

Wang X., Piao, S., Ciais, P., Friedlingstein, P., Myneni, R.B., Cox, P., Heimann, M., Miller, J., Peng, S., Wang, T., Yang, H. & Chen, A. (2014). A two-fold increase of carbon cycle sensitivity to tropical temperature variations. *Nature*, 506, 212-215. https://doi.org/10.1038/nature12915

Warneke, T., Messerschmidt, J., Notholt, J., Weinzierl, C., Deutscher, N., Petri, C., Grupe, P., Vuillemin, C., Truong, F., Schmidt, M., Ramonet, M. & Parmentier, E. (2017). TCCON data from Orleans, France, Release GGG2014R0. *TCCON data archive, CaltechDATA*. https://doi.org/10.14291/tccon.ggg2014.orleans01.R0/1149276

Washenfelder, R. A., Toon, G. C., Blavier, J.-F., Yang, Z., Allen, N. T., Wennberg, P. O., Vay, S. A., Matross, D. M. & Daube, B. C. (2006). Carbon dioxide column abundances at the Wisconsin Tall Tower site. *Journal of Geophysical Research*, 111, D22305. doi:10.1029/2006JD007154

Wennberg, P. O., Wunch D., Roehl C., Blavier J.-F., Toon G. C., Allen N., Dowell P., Teske K., Martin C. & Martin J. (2017). TCCON data from Lamont, Oklahoma, USA, Release GGG2014R1. *TCCON data archive, hosted by CaltechDATA*. https://doi.org/10.14291/tccon.ggg2014.lamont01.R1/1255070

Wennberg, P. O., Wunch D., Roehl C., Blavier J.-F., Toon G. C. & Allen N.(2017). TCCON data from California Institute of Technology, Pasadena, California, USA, Release GGG2014R1. *TCCON data archive, CaltechDATA*. https://doi.org/10.14291/tccon.ggg2014.pasadena01.R1/1182415

Wennberg, P. O., Roehl, C., Wunch, D., Toon, G. C., Blavier, J.-F., Washenfelder, R., Keppel-Aleks, G., Allen, N. & Ayers, J.(2017). TCCON data from Park Falls, Wisconsin, USA, Release GGG2014R1. *TCCON data archive, CaltechDATA*. http://doi.org/10.14291/tccon.ggg2014.parkfalls01.R1

Wofsy, S.C. , Goulden, M. L., Munger, J.W., Fan, S.M., Bakwin, P.S., Daube, B.C., Bassow, S.L. & Bazzaz, F.A. (1993). Net Exchange of CO_2 in a Mid-Latitude Forest. *Science (New York, N.Y.)*. 260. 1314-7. https://doi.org/10.1126/science.260.5112.1314

Wunch, D., Mendonca, J., Colebatch, O., Allen, N., Blavier, J.-F. L., Springett, S., Worthy, D., Kessler, R. & Strong, K. (2017). TCCON data from East Trout Lake, Canada, Release GGG2014R1. *TCCON data archive, CaltechDATA*. https://doi.org/10.14291/tccon.ggg2014.easttroutlake01.R1

Wunch, D., Toon, G. C., J.-F.L, Blavier, Washenfelder, R. A., Notholt, J., Connor, B. J., Griffith, D. W. T., Sherlock, V. & Wennberg, P. O. (2011). The Total Carbon Column Observing Network. *Philosophical Transactions of the Royal Society A*, 369, 2087–2112. https://doi.org/10.1098/rsta.2010.0240

Wunch, D., Toon, G. C., Wennberg, P. O., Wofsy, S. C., Stephens, B. B., Fischer, M. L., Uchino, O., Abshire, J. B., Bernath, P., Biraud, S. C., Blavier, J.-F. L., Boone, C., Bowman, K. P., Browell, E. V., Campos, T., Connor, B. J., Daube, B. C., Deutscher, N. M., Diao, M., Elkins, J. W., Gerbig, C., Gottlieb, E., Griffith, D. W. T., Hurst, D. F., Jiménez, R., Keppel-Aleks, G., Kort, E. A., Macatangay, R., Machida, T., Matsueda, H., Moore, F., Morino, I., Park, S., Robinson, J., Roehl, C. M., Sawa, Y., Sherlock, V., Sweeney, C., Tanaka, T. & Zondlo, M. A. (2010). Calibration

1055   of the Total Carbon Column Observing Network using aircraft profile data. *Atmospheric Measurement Techniques*, 3, 1351–1362. https://doi.org/10.5194/amt-3-1351-2010

Wunch, D., Toon, G. C., Sherlock, V., Deutscher, N. M., Liu, C., Feist, D. G. & Wennberg, P.O. (2015). Documentation for the 2014 TCCON Data Release. *CaltechDATA*.
1060   https://doi.org/10.14291/TCCON.GGG2014.DOCUMENTATION.R0/1221662

Wunch, D., Wennberg, P. O., Osterman, G., Fisher, B., Naylor, B., Roehl, C. M., O'Dell, C., Mandrake, L., Viatte, C., Griffith, D. W., Deutscher, N. M., Velazco, V. A., Notholt, J., Warneke, T., Petri, C., Maziere, M. D., Sha, M. K., Sussmann, R., Rettinger, M., Pollard, D., Robinson, J., Morino, I., Uchino, O., Hase, F., Blumenstock, T., Kiel, M.,
1065   Feist, D. G., Arnold, S. G., Strong, K., Mendonca, J., Kivi, R., Heikkinen, P., Iraci, L., Podolske, J., Hillyard, P. W., Kawakami, S., Dubey, M. K., Parker, H. A., Sepulveda, E., Rodriguez, O. E. G., Te, Y., Jeseck, P., Gunson, M. R., Crisp, D. & Eldering, A. (2017). Comparisons of the Orbiting Carbon Observatory-2 (OCO-2) XCO_2 measurements with TCCON. *Atmospheric Measurement Techniques*, 10(6), 2209-2238. https://doi.org/10.5194/amt-10-2209-2017.

1070   Yokota, T., Yoshida, Y., Eguchi, N., Ota, Y., Tanaka, T., Watanabe, H. & Maksyutov, S. (2009). Global concentrations of CO_2 and CH4 retrieved from GOSAT: First preliminary results. Scientific *Online Letters on the Atmosphere*, 5(1), 160-163. https://doi.org/10.2151/sola.2009-041

Zeng, N., Mariotti, A. & Wetzel, P. (2005). Terrestrial mechanisms of interannual CO_2 variability. *Global Biogeochemical Cycles*, 19, GB1016. https://doi.org/10.1029/2004GB002273